CO$_2$ Methanation on Supported Rh Nanoparticles: The combined Effect of Support Oxygen Storage Capacity and Rh Particle Size

Georgia Botzolaki [1], Grammatiki Goula [1], Anatoli Rontogianni [1], Ersi Nikolaraki [1], Nikolaos Chalmpes [2], Panagiota Zygouri [2], Michalis Karakassides [2], Dimitrios Gournis [2], Nikolaos Charisiou [3], Maria Goula [3], Stylianos Papadopoulos [4] and Ioannis Yentekakis [1,*]

[1] Laboratory of Physical Chemistry & Chemical Processes, School of Environmental Engineering, Technical University of Crete, GR-73100 Chania, Greece; gmpotzolaki@isc.tuc.gr (G.B.); mgoula@science.tuc.gr (G.G.); anatolirontogianni@gmail.com (A.R.); enikolaraki@yahoo.gr (E.N.)

[2] Department of Materials Science and Engineering, University of Ioannina, GR-45110 Ioannina, Greece; chalmpesnikos@gmail.com (N.C.); pzygouri@gmail.com (P.Z.); mkarakas@uoi.gr (M.K.); dgourni@uoi.gr (D.G.)

[3] Department of Chemical Engineering, University of Western Macedonia, GR-50100 Koila, Greece; ncharis@teiwm.gr (N.C.); maria.goula65@gmail.com (M.G.)

[4] Intergeo Ltd., Thermi, GR-57001 Thessaloniki, Greece; stelios.papadopoulos@intergeo.com

* Correspondence: yyentek@isc.tuc.gr; Tel.: +30-28210-37752

Abstract: CO$_2$ hydrogenation toward methane, a reaction of high environmental and sustainable energy importance, was investigated at 200–600 °C and H$_2$/CO$_2$ = 4/1, over Rh nanoparticles dispersed on supports with different oxygen storage capacity characteristics (γ-Al$_2$O$_3$, alumina-ceria-zirconia, and ceria-zirconia). The effects of the support OSC and Rh particle size on reaction behavior under both integral and differential conditions were investigated, to elucidate the combined role of these crucial catalyst design parameters on methanation efficiency. A volcano-type variation of methanation turnover frequency was found in respect to support OSC; Rh/ACZ, with intermediate OSC, was the optimal catalyst. The structure sensitivity of the reaction was found to be a combined function of support OSC and Rh particle size: For Rh/γ-Al$_2$O$_3$ (lack of OSC) methanation was strongly favored on small particles—the opposite for Rh/CZ (high OSC). The findings are promising for rational design and optimization of CO$_2$ methanation catalysts by tailoring the aforementioned characteristics.

1. Introduction

Fossil fuels (coal, oil, and natural gas) remain the dominant source of energy in the industrial, commercial, residential, and transportation sectors. Besides the fact that fossil fuels are finite, fossil fuel utilization leads to the emission of tremendous quantities of CO$_2$ in the atmosphere: These have consequently risen from ~280 ppm before the industrial revolution to ~410 ppm nowadays. Moreover, it is predicted that the concentration of CO$_2$ may reach ~570 ppm by the end of the century, if urgent mitigating actions are not implemented. As is well understood, CO$_2$ is the dominant greenhouse gas and has the most significant contribution to the greenhouse effect, as well as in the concomitant global warming and climate change. Therefore, control of CO$_2$ emissions is a critical and urgent environmental issue [1–9]. A possible solution can be provided by energy models with a reduced environmental footprint that can also be combined with the so-called *cyclic economy* strategies [4,9–14]. Apart from

direct efforts for replacement of carbon-based fuels with renewable energy sources, CO_2 capture and storage (CCS) and utilization-recycling through its conversion to added-value products and fuels are nowadays among the approaches that receive intense research and technological interest [1–14].

The latter strategy actually concerns the catalytic hydrogenation of CO_2 toward a variety of hydrogenated products (including mainly methane or methanol, as well as higher hydrocarbons or alcohols, dimethyl ether and formic acid), depending on the catalyst and conditions used [1–14]. In general, high pressures, along with Cu-, Zn-, and Cu-Zn-based catalysts mainly lead to the formation of methanol [1–3,15,16], whilst atmospheric pressure conditions and platinum-group metal (PGM)-, Ni-, Fe- and Co-based catalysts mainly lead to the formation of methane [1–8,17–46], via the highly exothermic carbon dioxide methanation reaction (R1), also known as the *Sabatier reaction* [1,4,5].

$$CO_2 + 4H_2 \leftrightarrow CH_4 + 2H_2O, \; \Delta H_{298K} = -164.7 \, kJ/mol \qquad \text{(R1)}$$
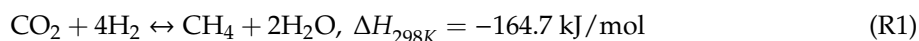
Methane is an energy carrier with a variety of applications in several sectors (residential, industrial, electrical energy power plants, and natural gas vehicles), due to the continuously growing natural gas distribution network. Bearing in mind that the hydrogen demands for CO_2 methanation (R1) can be provided via a solar- or wind-powered water-splitting system, we further expand the eco-friendly and sustainability character of a holistic CO_2 methanation concept. This concept, often called the *power-to-gas* process [4,11–14], attracts intense interest as a promising method for the storage of hydrogen, by overcoming the safety challenges of direct storage and transport technologies.

Kinetic and mechanistic studies of CO_2 methanation implicate either (i) CO_2 dissociation toward CO and O surface species, when the former interacts with hydrogen to produce methane [21,36,45,47], or (ii) interaction of adsorbed CO_2 and H species for the formation of adsorbed formate (HCOO) intermediates—part of these interact with adsorbed H to form CH_4, while the remaining desorbs, yielding CO [8,21,33,35,38,39,45–47]. However, the occurrence of the reverse water–gas shift (rWGS) reaction (R2) into the overall CO_2 methanation scheme is a critical factor which determines the products distribution, i.e., the selectivity toward CH_4 or CO [8,31,34,38,42,43,46]

$$CO_2 + H_2 \leftrightarrow CO + H_2O, \; \Delta H_{298K} = 41.1 \, kJ/mol \qquad \text{(R2)}$$
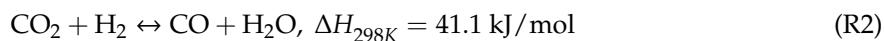
From a thermodynamic viewpoint, the CO_2 methanation reaction (R1) is exothermic; therefore, it is favored at low temperatures; above 600 °C, the Gibbs free-energy change of (R1) reaches positive values, and methane formation becomes unfavored [46]. However, low temperatures inhibit reaction rates. Thus, the development of methanation catalysts, active and selective at low temperatures, atmospheric pressure, and low H_2/CO_2 feed ratios remains a major challenge.

Among the CO_2 methanation catalysts investigated so far, supported PGM-catalysts (Pt, Pd, Rh, Ru, and Ir), in particular Rh and Ru, have been found to be highly active and selective at low temperatures and atmospheric pressure, even with low PGM-loadings (ca. 0.5 wt %) [30,32–46]. Non-precious metal alternatives (e.g., Ni, Fe, Co, or combinations of them) have also been investigated, with Ni being the most studied one, due to its good methanation activity and selectivity [17–31]. However, the propensity of Ni to form coke and to agglomerate when exposed to CH_4, CO, or CO_2-containing mixtures are major shortcomings of Ni-based catalysts [48–50]. In contrast, PGM-based catalysts exhibit very low propensity to accumulate carbon and to agglomerate [51–53], which justifies renewed interest on these catalysts for CO_2 methanation and hydrocarbon-processing studies.

In an attempt to tackle methanation catalysts' performance deficiencies on activity, selectivity and/or stability, several promotion approaches have been employed (examples include References [42, 43,46]), implicating surface-induced, support-mediated, or even electrochemical promotion routes, similar to those successfully applied in other catalytic systems (examples include References [54–57]). The advanced single-atom catalysis approach [37,58], found to work well in other CO_2 processing reaction systems (e.g., in the dry-reforming of methane (DRM) [59]), could also be a potential alternative for preparing high-performance CO_2 methanation catalysts. However, this should not

be considered, at least in advance, beneficial to methane formation; CO_2 methanation has been reported as a structure-sensitive reaction (examples include References [22,35,40,44]), where particle size affects methanation efficiency in a way that still remains unclear, often found to be favored on larger particles [35,40,44]. Evidently, any further insight elucidating what are the main material properties and how they interact, affecting the structural sensitivity of the reaction, will provide advantages and benefits for the design and optimization of CO_2 methanation catalysts.

Numerous efforts for promoting CO_2 methanation performance of supported metal catalysts by means of support-mediated promotion routes, using supports different than the traditional γ-Al_2O_3, can be found in the literature. These were TiO_2, SiO_2, MgO, ZrO_2, CeO_2, CeO_2-Al_2O_3, Ce-Zr-O, Ce-Zn-O, YSZ, LaO_x, PrO_x, MCM-41, or SBA-15 and applied to the group of VIII-XI metals, with the vast majority to Ni [17–27], some to Ru [35,42,43,45,46] and fewer to Rh [35,41], Pt [35,36], Pd [32,35], or Ir [44]. Although γ-Al_2O_3 is typically a good support, some performance improvements have been achieved, particularly by using TiO_2. It should be stressed here that the CO_2 hydrogenation reaction requires two different functionalities in an active catalyst: centers active in H_2 dissociation (typically reduced metal sites) and centers capable of activating CO_2 dissociation (typically support sites in ultimate contact with the metallic component of the catalyst) [26,27,37,38]. In such a complex catalytic system, even the Al_2O_3 oxide can function as a critical active catalyst component, as demonstrated by Kwak and co-workers [37,38]. It is also worth noting that, although Rh is one of the most active methanation catalysts [5,32,35], support-mediated promotion efforts on Rh-catalyzed CO_2 methanation have received less attention than those on Ni or Ru. Moreover, apart from a few studies on Ni-based catalysts [24–27], no particular emphasis has been given so far on critical support-mediated effects that can be offered by CeO_2-based mixed oxides via their enhanced oxygen storage capacity (OSC), O^{2-} mobility, reducibility (shuttling between Ce^{3+} and Ce^{4+} states), and concentration of surface oxygen vacancies' properties [60,61]. These properties have been found to play a pivotal role in many other catalytic applications, for example, in three-way catalytic converters (TWCs) [62], in hydrocarbons reforming, and water–gas shift reactions [49,50,52,53,63], and it is therefore reasonable to expect that they will be critical in a methanation reaction, as well. CeO_2-containing catalysts can typically provoke benefits on the required bi-functional operation of CO_2 methanation reaction, in which abundant oxygen vacancies on the support surface participate as CO_2 activation (adsorption and dissociation) sites [24–27,53]. Besides the above, a significant additional benefit has been recently demonstrated by the use of CeO_2-based mixed oxides as catalysts' supports: Owing to their high oxygen ion lability/mobility and the associated metal–support interactions, they were found to effectively stabilize catalysts' nanostructure, preventing thermal sintering of dispersed metal nanoparticles, or even facilitating particles redispersion at high temperatures [52,64,65].

In light of the above, the objective of this study was to explore, for the first time, the combined impact of the oxygen ion lability (or lack of it) characteristic of supporting materials with the mean particle size of the active metal on the Rh-catalyzed CO_2 methanation, in an attempt to gain advantages in the design of high-performance CO_2 methanation catalysts. The former characteristic is related to the OSC and O^{2-} mobility of the supports, which determine their propensity to provide O^{2-} spillover to catalyst nanoparticles, creating an *effective double layer*, [$O^{\delta-}$, δ^+], that strongly modifies their intrinsic activity toward catalytic reactions [53,57,66]. It is noted that different mean Rh particle sizes were obtained via the recently reported oxidative thermal sintering–redispersion method, which allows for an easy tuning of particle sizes at nanoscale [65]. Specifically, we report on the intrinsic and integral CO_2 methanation activity and selectivity of different sizes Rh nanoparticles deposited on oxide supports encompassing a wide range of OSC, namely γ-Al_2O_3, alumina–ceria–zirconia (ACZ: 80 wt % Al_2O_3–20 wt % $Ce_{0.5}Zr_{0.5}O_{2-\delta}$), and ceria-zirconia (CZ: $Ce_{0.5}Zr_{0.5}O_{2-\delta}$), in a comparative manner. For the sake of a rational comparison, the Rh/γ-Al_2O_3, Rh/ACZ, and Rh/CZ catalysts were exposed to the reaction mixture (CO_2+H_2), keeping the *effective mean contact time* of the reactants with catalyst active sites constant [56,67], rather than the weight-basis gas hourly space velocity (wGHSV; F/w). A strong, but non-monotonic effect of OSC of the support on Rh methanation activity was found:

Rh dispersed on the support with moderate OSC value (Rh/ACZ) was superior in CO_2 methanation. Moreover, a strong dependence of CO_2 methanation on Rh particle size was observed, with a very interesting feature of this structure sensitivity: For Rh particles dispersed on a non-reducible support (i.e., Rh/γ-Al_2O_3), the lower the particle size, the more superior the methanation performance, in full contrast with the feature for rhodium particles dispersed on high OSC support (i.e., Rh/CZ), where the higher the particle size, the more superior the methanation performance. These observations open up new possibilities on improving the methanation efficiency of supported metal catalysts by simultaneous adjusting their OSC and particle size characteristics. The results are adequately rationalized in terms of the ($O^{\delta-}$, δ^+) *effective-double-layer* account of promotion and metal–support interactions.

2. Results and Discussion

2.1. Morphological and Reducibility Characteristics of the Materials

Table 1 displays the main morphological and physicochemical properties of the support and catalysts studied herein. The BET surface area values (S_{BET}) of the oxide supports are 178, 149, and 22 m^2/g for the γ-Al_2O_3, ACZ, and CZ, respectively. After Rh deposition, the obtained counterpart catalysts show a slight decreased in S_{BET} values (160, 136, and 17 m^2/g, respectively), probably due to some pore blocking of the mesoporous oxide supports [65]. Minor losses on the BET surface area can also be observed in the catalysts subjected to further treatment at high temperatures, 750 and 850 °C, under oxidative conditions (Table 1). Rhodium metal loadings measured by ICP-OES was found to be close to the nominal 1 wt % Rh loading (Table 1) [53].

Table 1. Characteristics and properties of supports and the counterpart Rh catalysts (fresh or treated at high-temperature oxidative conditions: 750 or 850 °C).

Supports and Catalysts	Rh Content (wt %) [a]	S_{BET} (m^2/g)	Reducibility Characteristics		Mean Rh Particle Size (nm) [b]
			Total OSC (μmol O_2/g)	Redox Temperature Region and (Main Peaks) (°C) [b]	
Supports					
γ-Al_2O_3		178	0	-	-
ACZ		149	101	400–750 (500, 650)	-
CZ		22	557	300–850 (425, 710)	-
Rh nanoparticle Catalysts on γ-Al_2O_3					
Rh(1.2nm)/γ-Al_2O_3 (fresh)	1.0	160	69	50–600 (150, 500)	1.2
Rh(1.6nm)/γ-Al_2O_3 (treated at 750 °C)	1.0	159	70	50–600 (175, 400)	1.6
Rh(2.1nm)/γ-Al_2O_3 (treated at 850 °C)	1.0	140	65	50–600 (215, 400)	2.1
Rh nanoparticle Catalysts on ACZ (ACZ: 80 wt %Al_2O_3_20 wt %$Ce_{0.5}Zr_{0.5}O_{2-\delta}$)					
Rh(1.7nm)/ACZ					
(fresh)	0.8	136	146	30–550 (75, 150, 450)	1.7
Rh nanoparticle Catalysts on CZ (CZ: $Ce_{0.5}Zr_{0.5}O_{2-\delta}$)					
Rh(5nm)/CZ (fresh)	0.8	17	589	35–600 (105, 175, 380)	5.0
Rh(2.3nm)/CZ (treated at 750 °C)	0.8	16	476	30–550 (65, 115, 340)	2.3
Rh(2.1nm)/CZ (treated at 850 °C)	0.8	15	327	30–450 (55, 90, 290)	2.1

[a] Rh content of the catalysts was measured by using ICP-OES. [b] Mean Rh particle sizes are the arithmetic mean values of those obtained via isothermal H_2-Chemisorption experiments and HRTEM images.

The total oxygen storage capacities (in $\mu mol\ O_2/g$) of the supports and Rh catalyst counterparts, assessed by H_2-TPR as the half of the total amount of consumed H_2 in the 25–850 °C temperature interval of the H_2 consumption profiles, are shown in Figure 1. The oxide supports γ-Al_2O_3, ACZ, and CZ used encompass a wide range of OSC values, i.e., 0, 101, and 557 $\mu mol\ O_2/g$, respectively (Table 1), reflecting the non-reducibility of γ-Al_2O_3, and the $Ce^{4+} \rightarrow Ce^{3+}$ reduction of ACZ and CZ supports appearing in the TPR spectra (Figure 1a) as two overlapping broad peaks at ca. 300–550 °C and 500–850 °C, a feature characteristic of ceria-containing samples [68,69].
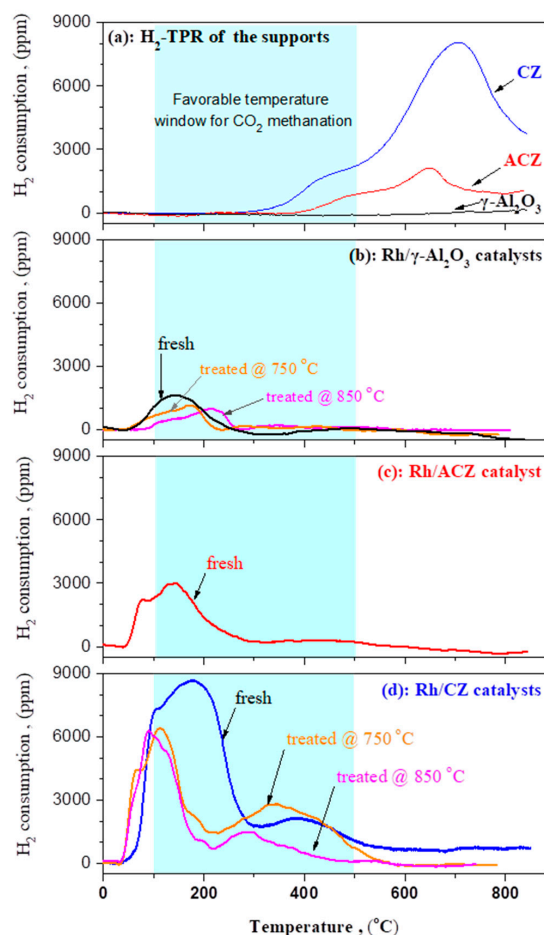
Figure 1. H_2-TPR profiles of (**a**) the γ-Al_2O_3, ACZ, and CZ supports; (**b**) fresh, treated at 750 °C, and treated at 850 °C Rh/γ-Al_2O_3 catalysts; (**c**) fresh Rh/ACZ catalyst; (**d**) fresh, treated at 750 °C, and treated at 850 °C Rh/CZ catalysts.

Incorporation of ~1 wt % Rh on the supports increases the OSC of the resulted catalysts to 69, 146, and 589 $\mu mol\ O_2/g$ of the fresh Rh/γ-Al_2O_3, Rh/ACZ, and Rh/CZ catalysts (Table 1 and Figure 1a). The corresponding 69, 45, and 32 $\mu mol\ O_2/g$ OSC increments found reflect the contribution of Rh^{3+} and Rh^{1+} oxide reduction to $Rh°$ and are close to the theoretically calculated amounts of O_2 for these transformations (i.e., 72 $\mu mol\ O_2/g$ for $Rh^{3+} \rightarrow Rh°$ and 29 $\mu mol\ O_2/g$ for $Rh^{1+} \rightarrow Rh°$), bearing in mind that Rh particles anchored on γ-Al_2O_3 can be fully oxidized (Rh^{3+}) in contrast to those dispersed on high OSC supports, which undergo only partial oxidation due to strong interactions between Rh particles and the support that destabilize rhodium oxide phases, as demonstrated by recent XPS studies [53].

It should be stressed, however, that incorporation of Rh on the supports resulted in a significant promotion of the reducibility of ACZ and CZ, as evidenced by the substantial shifts of the TPR peaks, attributed to the reduction of ceria at much lower temperatures (from ca. 300 to 850 °C for the supports $\rightarrow$ ca. 50–550 °C for the counterpart catalysts (Figure 1a,c,d and Table 1), indicating the strong promotion

of H_2 spillover [68,69], which, in the absence of metal, is limited by H_2 dissociation. These shifts are advantageous for the catalytic system under investigation, as the reducibility (i.e., the lattice oxygen lability) of the resulted Rh catalysts is well matched to the favorable temperature range of the CO_2 methanation reaction (Figure 1).

Some additional features of the H_2-TPR profiles are of particular interest. In the case of *fresh* Rh/γ-Al_2O_3 catalyst, the reduction of Rh species appeared as a LT peak (at ~150 °C) and a HT broad one (at ~500 °C) (Figure 1b and Table 1); the former is attributed to the reduction of Rh_2O_3 species anchored on the Al_2O_3 surface, while the latter to the reduction of Rh oxide diffused into alumina and thus in strong interaction with it ($RhAl_xO_y$) [70]. The interesting point is that the TPR peak of Rh_2O_3 surface species of the samples that have aged at oxidative thermal conditions, Rh/γ-Al_2O_3-*treated at 750 °C*, and Rh/γ-Al_2O_3-*treated at 850 °C*, is shifted to higher temperatures, from 150 to 175 and 215 °C, respectively (Figure 1b and Table 1), implying more difficult-to-reduce Rh particles—most probably larger particles. As discussed below, this is in agreement with the Rh particle agglomeration found after oxidative thermal aging of Rh particles anchored on γ-Al_2O_3 support, which is lacking in oxygen storage capacity. In striking contrast, TPR peaks on *fresh* Rh/CZ catalyst attributed to Rh oxide species (at ~105 °C), to superficial reduction of ceria taking place at CZ surfaces (at ~175 °C), and to the reduction of bulk ceria (at ~380 °C) are all shifted to lower temperatures over the thermally aged Rh/CZ catalysts (Figure 1d and Table 1). This implies an enhanced promotion of the reducibility of the aged (Rh/CZ-*treated at 750 °C* and Rh/CZ-*treated at 850 °C*), which is rationally understood by considering an enhanced metal–support interaction between Rh particles and CZ support resulting from a larger amount of undercoordinated rhodium sites, implying lower-size Rh particles (i.e., Rh redispersion during oxidative thermal aging). The latter is fully consistent with our results for the mean Rh particle sizes obtained by means of TEM and H_2-chemisorption experiments, included in Table 1 and discussed below.

Finally, the moderate reduction on the OSC values found for the thermally aged Rh/CZ catalysts (from 589 on *fresh* → 476 on *treated at 750 °C* → 327 μmol O_2/g on *treated at 850 °C*; Table 1 and Figure 1d) was expected, since it is well-known in the literature for CeO_2-ZrO_2 systems [71]. However, as will be discussed below, the remaining OSC ability of the catalysts is still high enough to induce substantial modifications on their CO_2 methanation performance.

Rh nanoparticle sizes measured by both HRTEM (Supplementary Materials Figure S1) and H_2 isothermal chemisorption, the arithmetic mean value ($\bar{d}_{Rh}$) obtained by the two independent methods for each catalyst (Supplementary Materials Section S1), are shown in Table 1. These take the values of 1.2, 1.7, and 5.0 nm on the fresh Rh/γ-Al_2O_3, Rh/ACZ, and Rh/CZ catalysts, respectively. It is highlighted that Rh nanoparticles dispersed on zero OSC support (γ-Al_2O_3) underwent agglomeration after high-temperature oxidative treatment under the sintering protocols #1 and #2: from 1.2 nm on Rh/γ-Al_2O_3 (*fresh*) → 1.6 nm on Rh/γ-Al_2O_3 (*treated at 750 °C*) → 2.1 nm on Rh/γ-Al_2O_3 (*treated at 850 °C*). In contrast, Rh nanoparticles on the high OSC support (CZ) underwent significant redispersion: from 5.0 nm on Rh/CZ (*fresh*) → 2.3 nm on Rh/CZ (*treated at 750 °C*) → 2.1 nm on Rh/CZ (*treated at 850 °C*). These findings are strikingly consistent with the H_2-TPR behavior of the corresponding samples (Figure 1).

The resistance to sintering during oxidative thermal treatment—on both mechanisms of particles agglomeration, i.e., large particle migration and coalescence (PMC) and Ostwald ripening (OR)—or even redispersion of metal particles dispersed on supports characterized by moderate and high values of labile lattice oxygen capacity has been thoroughly interpreted in Reference [65]; only a brief description is included herein. The creation of an $O^{\delta-}$ electric layer via the spontaneous (thermally driven) O^{2-} backspillover from the support to the surface of metal particles quenches the PMC mechanism due to the resulting interparticle electrostatic repulsion (anti-PMC). At the same time, metal atoms possibly detached from large metal crystallites are efficiently trapped by surface oxygen vacancies in the support material suppressing surface diffusion of these atomic species on the support and their subsequent attachment to larger particles (anti-OR). The latter can certainly lead to redispersion, the extent of

which depends on several factors, including the metal identity, the sintering conditions, and length of time imposed, and mainly the population of the surface oxygen vacancies of the support [65]. Metal nanoparticles dispersed on supports with a lack of labile lattice oxygen (e.g., γ-Al_2O_3) where such phenomena are absent provide little or no resistance to sintering under high-temperature oxidative treatment, as indeed found (Table 1).

2.2. Comparative Evaluation of Catalytic Performance: Effect of the Support

2.2.1. CO$_2$ Hydrogenation Performance Under Integral Reaction Conditions

Figure 2 depicts the CO_2 hydrogenation output characteristics, i.e., CO_2 conversion (Figure 2a), and the yields of methane (Y_{CH4}, Figure 2b) and CO (Y_{CO}, Figure 2c), and the corresponding CH_4 and CO selectivities (Figure 2d) as a function of reaction temperature (light-off performance), over the Rh(1.6nm)/γ-Al_2O_3, Rh(1.7nm)/ACZ, and Rh(2.1)/CZ catalysts, selected from the seven prepared samples (Table 1) so that to have different supporting material, but as close as possible to the mean Rh particle size. The latter was adopted to allow us to investigate and understand the effect of the support OSC isolated from that of particle size. For the sake of comparison, the equilibrium CO_2 conversion, CH_4 and CO yields, and selectivity profiles, predicted by the thermodynamics of the methanation reaction (R1) by using the Outokumpu HSC Chemistry® program [46], are also included in the figure. The feed composition was kept constant at the stoichiometry of the CO_2 methanation reaction (R1), i.e., 5% CO_2/20% H_2 balance Ar at 1 bar, as well as the *effective mean contact time* of the reactants, with rhodium active sites at $\tau(CO_2) = 1.26$ s (and $\tau(H_2) = 5.04$ s). Due to the different concentration of Rh active sites per mass of catalyst of the Rh(1.6nm)/γ-Al_2O_3, Rh(1.7nm)/ACZ, and Rh(2.1nm)/CZ samples, the latter was achieved by adjusting the total flow rates at 78, 60, and 47 N mL/min, respectively.
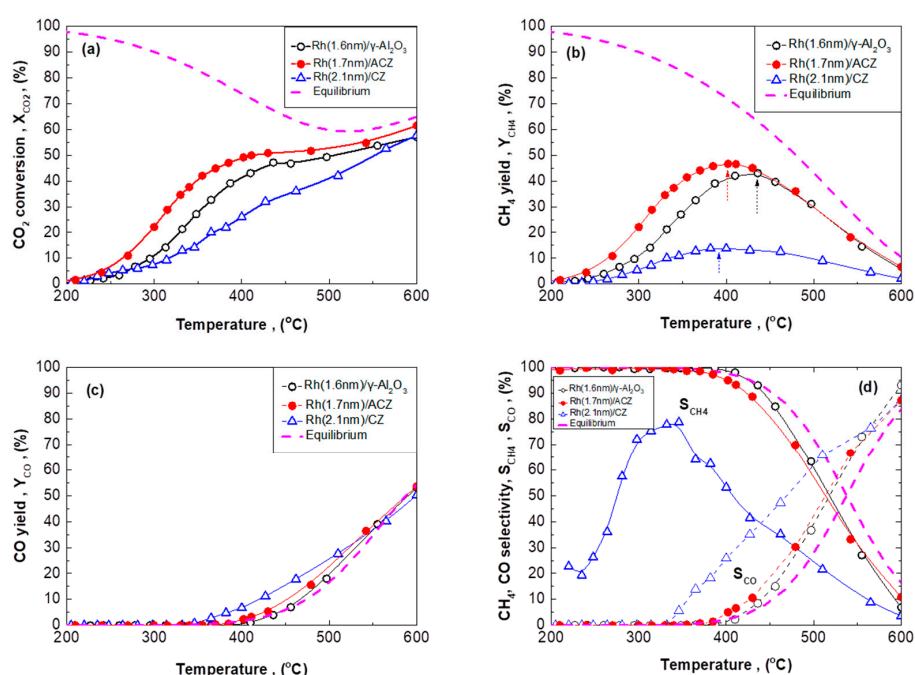

Figure 2. Conversion of CO_2 (**a**), methane yield (**b**), CO yield (**c**), and selectivities toward CH_4 and CO (**d**) as a function of temperature over the Rh(1.6 nm)/γ-Al_2O_3, Rh(1.7 nm)/ACZ, and Rh(2.1 nm)/CZ catalysts obtained under integral reaction conditions. Experimental conditions: feed composition of 5% CO_2/20% H_2/75% Ar at 1 bar; mass of catalyst $m_{cat} = 50$ mg; fixed mean contact time of CO_2 at $\tau(CO_2) \sim 1.3$ s (see text for discussion), corresponding to wGHSV values of 93,600, 72,000, and 56,400 N mL/g·h for the Rh(1.6 nm)/γ-Al_2O_3, Rh(1.7 nm)/ACZ, and Rh(2.1 nm)/CZ catalysts, respectively.

At the relatively high wGHSVs employed (ca. 56400–93600 N mL/g·h; low effective mean contact time $\tau(CO_2)$~1.3 s), the CO_2 hydrogenation reaction is practically activated at temperatures higher than ~180–200 °C for all three catalysts tested (Figure 2a); then CO_2 conversion increases with a temperature approaching the thermodynamic equilibrium curve at about 550 °C. The clear superiority of Rh particles dispersed on ACZ support (with intermediate OSC = 101 µmol O_2/g) on CO_2 conversion efficiency is evident in the whole temperature range investigated (200–600 °C), while Rh particles on CZ support (with the highest OSC = 557 µmol O_2/g) appear worse, even compared with Rh particles dispersed on γ-Al_2O_3 with negligible oxygen storage capacity and lability. Interesting differences in the CH_4 and CO product distribution features between the three catalysts are also perceivable (Figure 2b,c). Compared with γ-Al_2O_3, the most active Rh(1.7 nm)/ACZ catalyst effectively promotes CH_4 yield (i.e., the CO_2 methanation reaction (R1)) at temperatures up to ~425 °C, while at higher temperatures, its Y_{CH4} profile approaches that of Rh(1.6nm)/γ-Al_2O_3. On the other hand, the methanation efficiency of Rh(2.1 nm)/CZ appears significantly depressed and inferior to that of Rh(1.6 nm)/γ-Al_2O_3 in the whole temperature range. Finally, maximum methane yield values obtained for Rh(1.7 nm)/ACZ, Rh(1.6 nm)/γ-Al_2O_3, and Rh(2.1 nm)/CZ were 46.8% (at 402 °C), 43.3% (at 436 °C), and 14.2% (at 388 °C), respectively (Figure 2b; Table 2).

Table 2. Support-mediated promotion characteristics, apparent activation energies, and pre-exponential factors for CO_2 methanation reaction over Rh(1.6nm)/γ-Al_2O_3, Rh(1.7nm)/ACZ, and Rh(2.1nm)/CZ catalysts with different OSC of their supports.

Catalyst	Support OSC (µmol O_2/g)	$Y_{CH4,max}$ (%)	$T@Y_{CH4,max}$ (°C)	TOF_{CH4} Apparent Activation Energy (E_a) (kJ/mol)	Pre-Exponential Factor $\left(TOF^o_{CH4}\right)$ (s^{-1})
Rh(1.6nm)/γ-Al_2O_3	0	43.3	436	70.5 ± 1.9	12.4 ± 0.4
Rh(1.7nm)/ACZ	101	46.8	402	75.0 ± 2.8	14.1 ± 0.6
Rh(2.1nm)/CZ	557	14.2	388	87.5 ± 3.5	15.3 ± 0.8

According to thermodynamics, CH_4 yield is restricted at elevated temperatures (Figure 2b), while the Gibbs free-energy of the methanation reaction (R1) receives positive values at temperatures higher than 600 °C. Therefore, getting close to this temperature (typically for T > ~400 °C; Figure 2b), the initially increasing Y_{CH4} passes through a maximum and then lessens, approaching the equilibrium predicted profile. On the other hand, as expected and shown in Figure 2c, CO production is activated at elevated temperatures (ca. 350–400 °C) where the reverse water–gas shift (rWGS) reaction is thermodynamically favored. Then, it keeps increasing upon increasing temperature at the expense of CH_4 production, thus rendering the "*CO_2 methanation system*" to a "*syngas production system*" (Figure 2b–d). It is also evident that the Y_{CO} profile is systematically moved to lower temperatures as the support's OSC increases (Figure 2c). Thus, CO productivity for each catalyst is ignited according to the following temperature order: 350 °C (over Rh(2.1nm)/CZ) < 375 °C (over Rh(1.7nm)/ACZ) < 410 °C (over Rh(1.6nm)/γ-Al_2O_3), i.e., in reverse order, compared to the order of the OSC values of the supports, OSC(CZ) = 557 µmol O_2/g > OSC(ACZ) = 101 µmol O_2/g > OSC(γ-Al_2O_3) = 0 µmol O_2/g. A notable effect of the OSC of the support on the Rh-catalyzed rWGS reaction (R2) is therefore obvious; the higher the OSC of the support, the greater the promotion of rWGS reaction at elevated (> ~350 °C) temperatures.

The CH_4 and CO selectivity performances of the Rh(1.6nm)/γ-Al_2O_3 and Rh(1.7nm)/ACZ catalysts depicted in Figure 2d are in accordance with the CH_4 and CO productivity discussed above. They offer ~100% selectivity toward CH_4 (S_{CH4}) at the low- to intermediate-temperature range (200 to ~350 °C), while at higher temperatures, the selectivity toward CO (S_{CO}) starts increasing, with a concomitant S_{CH4} decrease, in accordance with thermodynamics. The symmetry between their S_{CH4} and S_{CO} curves in respect to the horizontal invisible line at $S = 50\%$, reflects the fact that no other products except CH_4

and CO were obtained by these two catalysts; the carbon balance $X_{CO2} = Y_{CH4} + Y_{CO}$ for these two catalysts always closed well with deviations of less than ~3 %.

Nevertheless, the selectivity behavior of Rh(2.1nm)/CZ appears to be rather more complicated. For this catalyst, the carbon balance, $X_{CO2} = Y_{CH4} + Y_{CO}$, did not close well, implying the formation of additional C-containing by-products, besides CH_4 and CO. Indeed, such C_{2+} products (mostly C_2H_6) were observed in gas chromatographs, but at very low concentrations, inappropriate for quantitative analysis within the detection limits of our analysis system. It is worth noting that formation of C_{2+} products in small amounts has been reported in the literature of CO_2 hydrogenation over Rh/TiO_2 and Rh/Nb_2O_5 catalysts with the main product being C_2H_6 [72]. An overview and thorough explanation of the effect of the support OSC on the catalysts' light-off and turnover frequency (TOF) performances is given below, following the presentation of the latter, since both should have a common interpretation.

2.2.2. CO_2 Hydrogenation Intrinsic Activity of Rh Nanoparticles

Turnover frequency results for the CO_2 methanation (TOF_{CH4}) on Rh(1.6nm)/γ-Al$_2$O$_3$, Rh(1.7nm)/ACZ, and Rh(2.1nm)/CZ are shown as Arrhenius plots in Figure 3; TOF_{CH4} is given as *moles of methane produced per mole of rhodium active site per second* (Rh active sites were estimated on the basis of mean Rh particle size values given in Table 1). Kinetic data were acquired under conditions of low CO_2 (and H_2) conversion, typically ~5–15%, in order to reflect intrinsic activity, unaffected by reactants concentration gradients, mass, and/or thermal transport constraints (differential reaction conditions). Apparently, Rh dispersed on ACZ with the intermediate OSC shows the highest methanation activity, followed by Rh on γ-Al$_2$O$_3$ and finally by Rh on CZ, with the higher OSC exhibiting the lower activity (Figure 3). Its TOF_{CH4} values are also positively compared with values recently reported for Rh catalysts supported on other supports and studied at similar conditions (examples include References [35,40]).
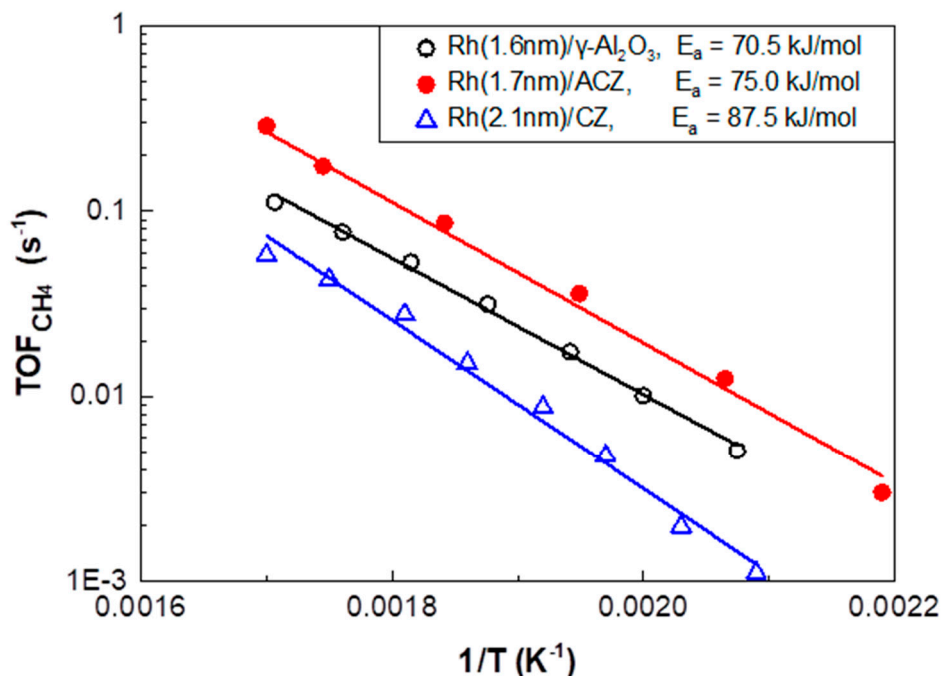

Figure 3. Arrhenius plots of the CH_4 formation turnover frequency (TOF_{CH4}) obtained for Rh(1.6nm)/γ-Al$_2$O$_3$, Rh(1.7nm)/ACZ, and Rh(2.1nm)/CZ catalysts obtained under differential reaction conditions (reactant conversions ~5–15%). Experimental conditions as in Figure 2.

The apparent activation energy (E_a) of the methanation reaction systematically increases upon increasing the OSC of the support, E_a = 70.5, 75.0, and 87.5 kJ/mol with concomitant increases of the

pre-exponential factor as well, TOF^o_{CH4} = 12.4, 14.1, and 15.3 s^{-1}, for Rh(1.6nm)/γ-Al$_2$O$_3$, Rh(1.7nm)/ACZ, and Rh(2.1nm)/CZ, respectively (Table 2). These apparent activation energy values are similar to previously reported values over supported Rh catalysts. Solymosi et al. [73] reported an apparent activation energy value of 68 kJ/mol on Rh/γ-Al$_2$O$_3$, while more recently Karelovic and Ruiz [40] reported an interesting dependence of E_a on Rh particle size for Rh/γ-Al$_2$O$_3$ catalysts, which varied in the range of 61–95 kJ/mol when Rh particle size varied between 3.6 and 15.4 nm with the smaller particles to obey the higher E_a values due to the structure sensitivity of the reaction, as the authors confirmed. On the other hand, in cases where Rh particles were dispersed on supports imposing significant metal–support interactions, such as TiO$_2$ and W^{6+}-doped TiO$_2$, elevated E_a values were typically obtained: 71 kJ/mol on Rh/TiO$_2$ [35] and 70–103 kJ/mol on Rh/(W^{6+}-doped TiO$_2$) [41] catalysts.

Taking into consideration both integral and intrinsic CO$_2$ hydrogenation performance of the Rh nanoparticles dispersed on the different supports, γ-Al$_2$O$_3$, ACZ, and CZ (Figures 2 and 3; Table 2), and given the large variation in oxygen ion lability between them that can stimulate possible metal–support interactions [53,66], the main experimental observations are summarized as follows:

(i) Supports possessing intermediate oxygen storage capacity and lability (ACZ) substantially promote the CO$_2$ methanation activity of Rh (Figure 2b, Figure 3, and Table 2), providing a volcano-type promotion behavior in respect to the OSC of the support or the counterpart catalyst (Figure 4).

(ii) ACZ and CZ promote the reverse water–gas shift reaction (CO formation) in a monotonic manner in respect to their OSC value; the higher the OSC, the higher the promotion of rWGS (Figure 2c). In particular, CZ also promotes the formation of additional C-containing byproducts, besides CH$_4$ and CO (Figure 2d).

(iii) The apparent activation energies (E_a) of CH$_4$ formation and the corresponding pre-exponential factors (TOF^o_{CH4}) increase monotonically with increasing the OSC of the support, i.e., E_a and TOF^o_{CH4} values follow the order Rh/CZ > Rh/ACZ > Rh/γ-Al$_2$O$_3$ (Figure 3; Table 2).
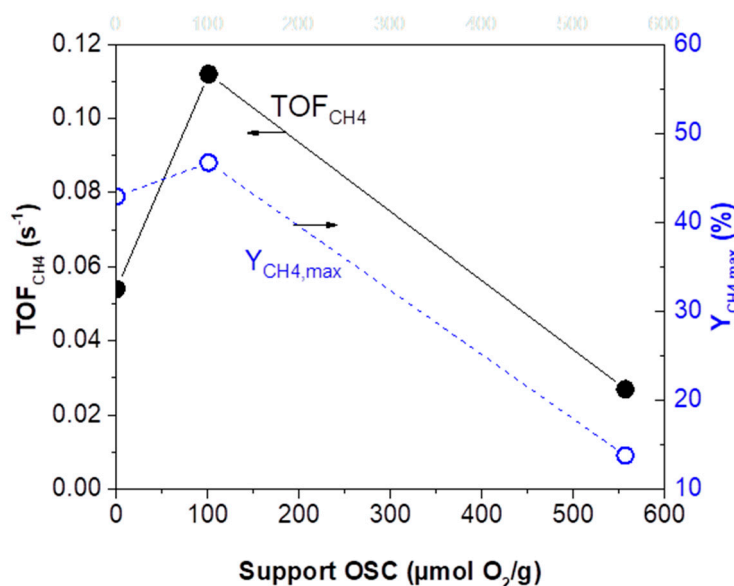

Figure 4. Dependence of methane turnover frequency (TOF_{CH4}) at T = 280 °C and maximum methane yield ($Y_{CH4,max}$) on support oxygen storage capacity. Experimental conditions as in Figures 2 and 3.

It is readily understood that the combination of the effects of (i) and (ii) determines the obtained Rh/ACZ > Rh/γ-Al$_2$O$_3$ > Rh/CZ order for the maxima in CH$_4$ yield and the temperatures where these maxima are located (Figure 2b and Table 2), as well as the behavior of the selectivity toward CH$_4$ and CO (Figure 2d). The question arising regards the origin of these effects. It has been previously demonstrated that CeO$_2$-based supports are characterized by substantial oxygen storage capacity

(Table 1) due to the labile lattice oxygen and therefore by high concentration of bulk and surface oxygen ion defects (oxygen vacancies, $V_{\ddot{O}}$) [57,60–62]. Therefore, the suggestion of a bi-functional reaction mechanism, commonly employed in mechanistic reaction schemes involving CO_2 processing over CeO_2-containing catalysts [53], is consistent with the present catalytic system as well.

According to this mechanism, CO_2 activation (dissociative adsorption) is especially favored on CeO_2-containing supports incorporating a significant concentration of oxygen vacancies ($V_{\ddot{O}}$) that act as additional active centers, via the reaction (R3) [53]:

$$CO_2\ (g) + V_{\ddot{O}} \rightarrow O_i^{\parallel} + CO\ (g) \tag{R3}$$

where $O_i^{\parallel}$ represents interstitial oxygen ion, i.e., O^{2-} corresponding to the redox cycle Ce^{3+}/Ce^{4+} characteristic of $CeO_2{}^-$ containing supports [60–62] the lability (and mobility) of which is determined by the equilibrium reaction (R4) taking place into the support body between lattice oxygen (O_O), interstitial oxygen ions ($O_i^{\parallel}$), and lattice oxygen vacancies ($V_{\ddot{O}}$) [57]:

$$O_O \leftrightarrow V_{\ddot{O}} + O_i^{\parallel} \tag{R4}$$

Such a contribution of the support to CO_2 activation (R3) should ultimately be beneficial for the overall methanation reaction progress. Specifically, the elevated population of surface oxygen vacancies on ACZ and CZ supports will substantially promote CO_2 scission with a concomitant effective promotion of the rWGS reaction (R2), a key step in the CO_2 methanation pathway. Therefore, the enhancement found in both Y_{CH4} and Y_{CO} yields on Rh/ACZ catalyst is fully consistent with the effect of its OSC characteristic on the CO_2 hydrogenation performance (Figure 2). The pronounced CO evolution (Y_{CO}) by Rh/CZ compared to Rh/ACZ (and even more compared to Rh/γ-Al_2O_3, Figure 2c) is a consequence of the higher availability of $V_{\ddot{O}}$ centers on the surface of CZ, resulting from its higher OSC, which facilitates reaction (R3). However, the inferior Y_{CH4} of the Rh/CZ still remains to be interpreted, and it can be readily understood as follows. An additional effect of the occurrence of reaction (R3) is the continuous replenishment of the support with interstitial O^{2-} ions ($O_i^{\parallel}$) that can spontaneously (thermally driven) backspillover onto the surface of Rh particles creating an effective double layer [$O^{\delta-}, \delta^+$] via the step (R5) [53,66]:

$$O_i^{\parallel} + Rh^* \rightarrow \left[O^{\delta-}, \delta^+\right]Rh^* + V_{\ddot{O}} \tag{R5}$$
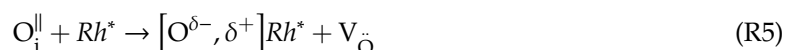
where Rh^* denotes a rhodium active site on the surface of Rh particles.

According to the *effective-double-layer* account of catalysts promotion and metal–support interactions [66] the as-created $O^{\delta-}$ layer on the surface of metal particles (Figure S2 in the Supplementary Material) acts as an electronic modifier of the catalytic particles by its compensating charge, δ^+, altering their work function and chemisorptive properties and hence the intrinsic activity and/or selectivity toward catalytic reactions [52,57,66,74], before the ultimate reaction of $O^{\delta-}$ species as *sacrificial* promoter ($O^{\delta-}$ species are quite reactive and therefore consumed by the oxidizable reactants (e.g., H_2) that scavenge them [66]). Nevertheless, they are effective because of their continuous replenishment via reactions (R3) and (R5). Apparently, the intensity of the $O^{\delta-}$ layer and consequently its concomitant effect on intrinsic activity are in accordance with the oxygen ions capacity and mobility of the support.

In this context, the increased work function, due to the creation of the effective double layer ([$O^{\delta-}, \delta^+$]), or equivalently the decreased electron availability on the surface of Rh particles, results in strengthening of the chemisorptive bond of electron donor (electrophobic) adsorbates and weakening that of electron acceptor (electrophilic). Nevertheless, CO adsorption characteristics on catalyst particles play a key role in CO_2 methanation mechanism [22,37,39]. CO chemisorption on Pt-group metals involves both donation and backdonation of electrons. Therefore, it is difficult to estimate which one of its electrophilic or electrophobic character dominates under the specific conditions employed, and therefore to quantify the effect of increasing metal work function on its chemisorption

bond strength [54,75] (additional information is provided in the Supplementary Materials, Section S2). The present results, however, point toward the electrophobic character of CO chemisorption bonding in agreement with References [75,76]. Indeed, the monotonic increase in the apparent activation energy of the methanation reaction upon increasing the OSC of the support (observation iii, Table 2), which is associated with the concomitant enhancement in intensity of the $O^{\delta-}$ layer, accompanied by the increasing work function of Rh, rationally implies a strengthening of the Rh-CO bond; that is, the electron-donor (electrophobic) character of CO dominates in our catalytic system under the conditions employed. More specifically, the increase in the apparent activation energy of the CO_2 methanation reaction indicates that the reaction proceeds through schemes with higher energetic barriers; a more strongly bonded, thus less reactive, CO is consistent with this observation. This view is also consistent with the observed increase of the entropic (TOF^o_{CH4}) Arrhenius factor (observation iii, Table 2): Strengthening of the Rh-CO bond implies an increase in the amount of adsorbed CO on the Rh surface, and therefore to an enhancement of the reaction probability, i.e., higher methanation rate, as indeed obtained (observation i). However, over-strengthening of the Rh-CO bond can finally induce self-poisoning of the reaction, i.e., CO-poisoning of the surface by strongly adsorbed, less-reactive CO, which is fully consistent with the inferior methanation activity of Rh/CZ and the concomitant volcano-type dependence of the promotion on the support's OSC (observation i; Figure 4). Apparently, the values of these two compensative factors (E_a and pre-exponential factor) of the methanation reaction (R1) are optimized when supports with intermediate OSC values (e.g., ACZ) are used.

Our recent post-DRM-reaction XPS studies on Rh/γ-Al_2O_3, Rh/ACZ, and Rh/CZ catalysts [53] have shown that, between the Rh^{3+}, Rh^{1+}, and Rh° oxidation states of rhodium, the principal Rh species was Rh°; its relative content decreasing in the order Rh/CZ(100%) > Rh/ACZ(72%) > Rh/γ-Al_2O_3(55%). That is, supports with high oxygen ion lability (ACZ and CZ) due to O^{2-} backspillover that weakens the Rh-O bond destabilize rhodium oxide, promoting its metallic state [53]. Bearing in mind that, under CO_2 hydrogenation and DRM reactions, the catalyst is exposed to a relatively close reaction products environment, and the bifunctional character of CO_2 methanation reaction, which requires reduced metal sites that are active in H_2 dissociation [26,27,37,38], it is reasonable to suggest that the increase in Rh° state on the catalyst containing ACZ and CZ supports is an additional factor promoting the methanation reaction however, minor in effect compared to the aforementioned one related to CO formation and its chemisorption strengthening on metal sites, able to create reverse effects (CO-poisoning) in the case of supports with very high OSC value (CZ).

The work of Liu et al. [24] on the effect of CeO_2 addition on Ni/Al_2O_3 catalyst for CO_2 methanation is worth mentioning here. By incorporating different amounts of CeO_2 between 0 and 6 wt %, the authors found that methanation is significantly promoted by low CeO_2 loadings, optimized at an intermediate loading of 2 wt %, and then depressed for higher CeO_2 loadings. The CeO_2-induced promotion was attributed to the enhanced reducibility of the resulted Ni/CeO_2-Al_2O_3 catalysts. Although the OSC values of their catalysts are not available for a closer comparison with the present results, the general feature of the reported promotion is in qualitative agreement with the volcano-type behavior found herein as a function of the OSC (reducibility) of our catalysts.

2.3. Effect of Rh Particle Size on CO_2 Methanation Performance

In this context, Rh/Al_2O_3 and Rh/CZ catalysts, as representative extreme cases regarding the OSC value of the supporting material, were selected for a detailed investigation of the effect of mean particle size of Rh on CO_2 methanation reaction, i.e., its structure sensitivity, and possible synergy with the OSC characteristic of the support.

2.3.1. Rh/γ-Al_2O_3 Catalysts with Different Mean Rh Particle Size

Figure 5 illustrates the CO_2 methanation performance (X_{CO2}, Y_{CH4}, Y_{CO}, S_{CH4}, and S_{CO}) of the three Rh/γ-Al_2O_3 catalysts different in the mean Rh particle size: 1.2, 1.6, and 2.1 nm. Although the range of particle size values does not show a large variation, the reaction apparently exhibits

structure sensitivity, clearly influencing CO_2 conversion (Figure 5a) and CH_4 yield (Figure 5b), but not to any significant extent the CO yield (Figure 5c), thus causing marginal effects on system selectivity (Figure 5d). Overall, CH_4 formation performance superiority follows the order Rh(1.2nm)/γ-Al_2O_3 > Rh(1.6nm)/γ-Al_2O_3 >> Rh(2.1nm)/γ-Al_2O_3; the reverse water–gas shift (rWGS) reaction appears insensitive to Rh particle size.
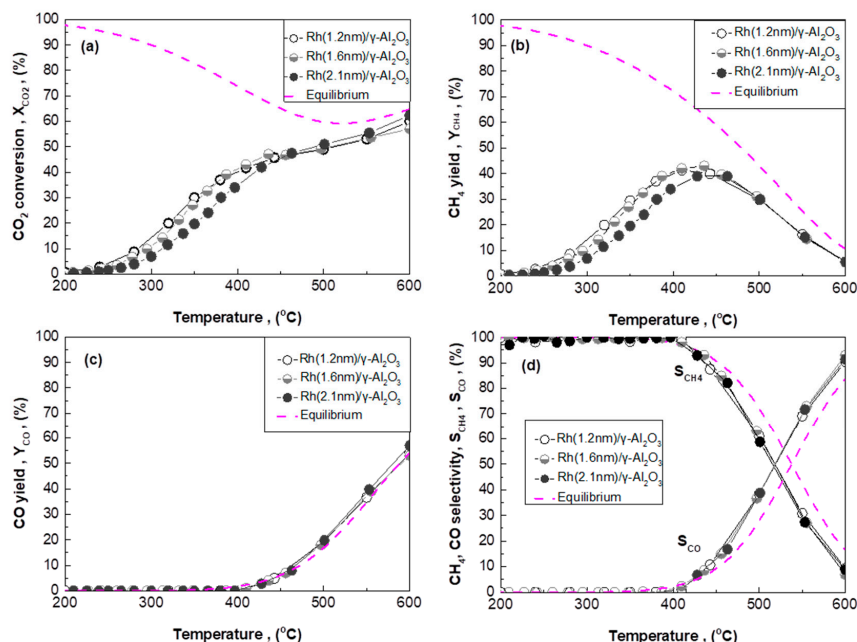
Figure 5. CO_2 hydrogenation performance (X_{CO2} (**a**), Y_{CH4} (**b**), Y_{CO} (**c**), S_{CH4} and S_{CO} (**d**)) of Rh(1.2nm)/γ-Al_2O_3, Rh(1.6nm)/γ-Al_2O_3, and Rh(2.1nm)/γ-Al_2O_3 catalysts under integral reaction conditions. Experimental conditions: feed composition of 5% CO_2/20% H_2/75% Ar at 1 bar; mass of catalyst m_{cat} = 50 mg; fixed mean contact time of CO_2 at $\tau(CO_2)$~1.3 s, corresponding to wGHSV values of 120,000, 93,600, and 70,800 N mL/g·h for the Rh(1.2nm), Rh(1.6nm), and Rh(2.1nm)/γ-Al_2O_3 catalysts, respectively.

Under intrinsic reaction conditions (Figure 6), the trend of methane formation turnover frequency (TOF_{CH4}) is similar to the above order, while an increasing trend of the apparent activation energy of the methanation reaction upon decreasing Rh particle size is obtained: 67.5 kJ/mol < 70.5 kJ/mol << 77.9 kJ/mol over Rh(1.2nm)/γ-Al_2O_3, Rh(1.6nm)/γ-Al_2O_3, and Rh(2.1nm)/γ-Al_2O_3, respectively (Figure 6 and Table 3).

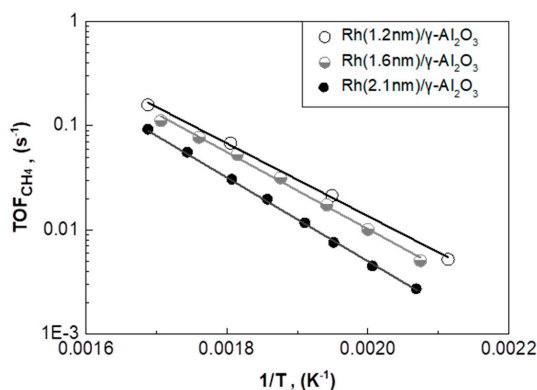**Figure 6.** Arrhenius plots of the CH_4 formation turnover frequency (TOF_{CH4}) obtained for Rh/γ-Al_2O_3 catalysts with different mean Rh particle size. Experimental conditions as in Figure 5.

Table 3. Apparent activation energies and pre-exponential factors for CO_2 methanation reaction over Rh/γ-Al$_2$O$_3$ catalysts with different mean Rh particle size, and *TOF$_{CH4}$* values at 280 °C.

Catalyst	Mean Rh Particle Size (nm)	*TOF$_{CH4}$* Apparent Activation Energy (E_a) (kJ/mol)	Pre-Exponential Factor $\left(TOF^o_{CH4}\right)$ (s^{-1})	*TOF$_{CH4}$* at T = 280 °C (s^{-1})
Rh(1.2nm)/γ-Al$_2$O$_3$	1.2	67.5 ± 1.5	12.0 ± 0.3	66.5·10^{-3}
Rh(1.6nm)/γ-Al$_2$O$_3$	1.6	70.5 ± 1.9	12.4 ± 0.4	54.0·10^{-3}
Rh(2.1nm)/γ-Al$_2$O$_3$	2.1	77.9 ± 0.7	13.4 ± 0.2	30.0·10^{-3}

The structure sensitivity of Rh/γ-Al$_2$O$_3$-catalysed CO_2 methanation is known in the literature. Studying Rh/γ-Al$_2$O$_3$ catalysts with a variety of Rh particle sizes (between 3.6 and 15.4 nm) obtained by applying different Rh loadings (between 1 and 5 wt %), Karelovic and Ruiz [40] reported significant structure sensitivity of the titled reaction, which was favored on larger Rh particles but only at low temperatures (135–150 °C). At a higher temperature (200 °C), the authors observed similar CH$_4$ formation TOFs on all Rh particle sizes, or slightly better on the smaller one. Here, we report a clear beneficial influence on CH$_4$ formation activity of the smaller particles at temperatures higher than 200 °C. Based on the facts that the catalysts studied herein concern small Rh particle sizes (1.2–2.1 nm), smaller than that in Reference [40], and the temperature window is higher than 200 °C (ca. 200–350 °C), the observed structure sensitivity and its trend are actually in agreement with that reported by Karelovic and Ruiz at similar conditions. An increasing variation of the apparent activation energy, in the range of ca. 61–95 kJ/mol, with decreasing the particle size was also reported by the authors [40]. Changes in E_a in the present study have an opposite trend: E_a is increased (up to 10 kJ/mol; Figure 6, Table 3) as the mean Rh particle size increases from 1.2 to 2.1 nm. The different trend compared to that found in Reference [40] most probably originates from the different reaction conditions applied, but also on possible differences on the individual particle distribution of the catalysts. More specifically, it is attributed to the fact that the thermal sintering method applied to our catalysts for changing the size of the particles leads to significantly narrow particle size distribution [65,77], as compared to methods employing different metal loadings to achieve this which commonly lead to a fairly broader particle size distribution.

2.3.2. Rh/CZ Catalysts with Different Mean Rh Particle Sizes

Figure 7 illustrates the full CO_2 methanation performance of Rh/CZ catalysts, in respect to variation in mean Rh particle size, between 2.1 to 5 nm. Apparently, the Rh/CZ catalyst exhibits rather stronger structure sensitivity than that previously depicted for Rh/γ-Al$_2$O$_3$ with the following principal features: The CO_2 conversion is significantly depressed with decreased size of Rh particles (Figure 7a), similarly to the CH$_4$ yield (Figure 7b), while only marginal effects are recorded in CO yield (Figure 7c). However, as has been already mentioned in Section 3.2.1, the selectivity behavior of the Rh/CZ catalysts appears to be rather more complicated, especially over Rh(2.1nm)/CZ with the lowest Rh particles size (Figure 7d), for which the carbon balance ($X_{CO2} = Y_{CH4} + Y_{CO}$) did not close well, implying the formation of additional C-containing byproducts besides CH$_4$ and CO [72]. Overall, as shown in Figure 7, the methanation superiority over Rh/CZ catalysts in relation to Rh particle size follows the order Rh(5nm)/CZ > Rh(2.3nm)/CZ > Rh(2.1nm)/CZ; the reverse water–gas shift (rWGS) reaction appears, again, rather insensitive to Rh particle size.
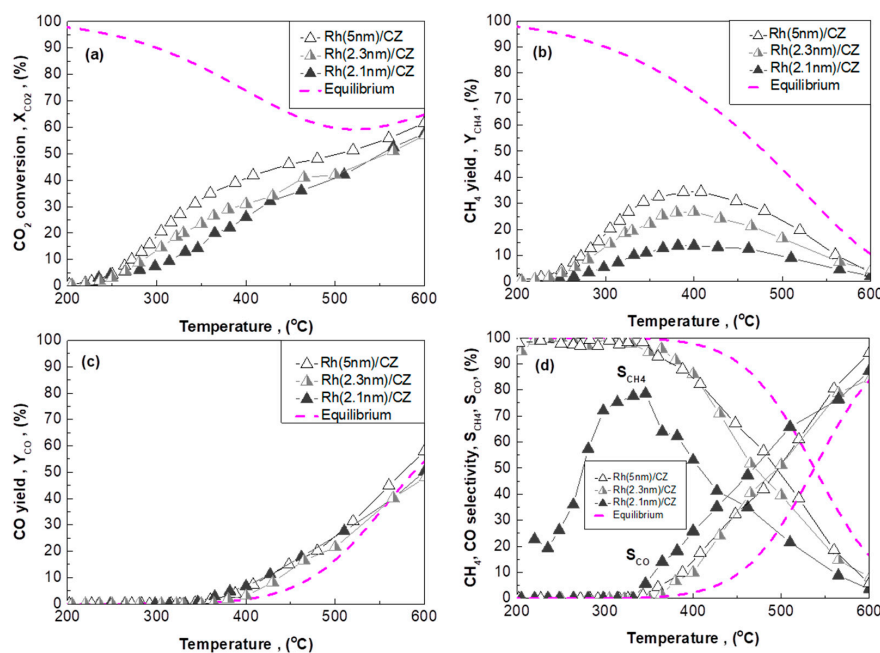
Figure 7. CO_2 hydrogenation performance (X_{CO2} (**a**), Y_{CH4} (**b**), Y_{CO} (**c**), S_{CH4} and S_{CO} (**d**)) of Rh(5nm)/CZ, Rh(2.3nm)/CZ, and Rh(2.1nm)/CZ catalysts under integral reaction conditions. Experimental conditions: feed composition of 5% CO_2/20% H_2/75% Ar at 1 bar; mass of catalyst m_{cat} = 50 mg; fixed mean contact time of CO_2 at $\tau(CO_2)$~1.3 s, corresponding to wGHSV values of 24,000, 50,400, and 56,400 N mL/g·h for the Rh(5nm), Rh(2.3nm), and Rh(2.1nm)/CZ catalysts, respectively.

The Arrhenius plots of the turnover frequency of methane formation (TOF_{CH4}) on Rh/CZ catalysts with different particle sizes (Figure 8) show a similar to the aforementioned methanation trend. Moreover, a slight decrease in the apparent activation energy upon decreasing Rh particle size is obtained: 83.6 kJ/mol < 85.8 kJ/mol < 87.5 kJ/mol over Rh(5nm)/CZ, Rh(2.3nm)/CZ, and Rh(2.1nm)/CZ catalysts, respectively, while the pre-exponential factor is marginally affected (Figure 8; Table 4).
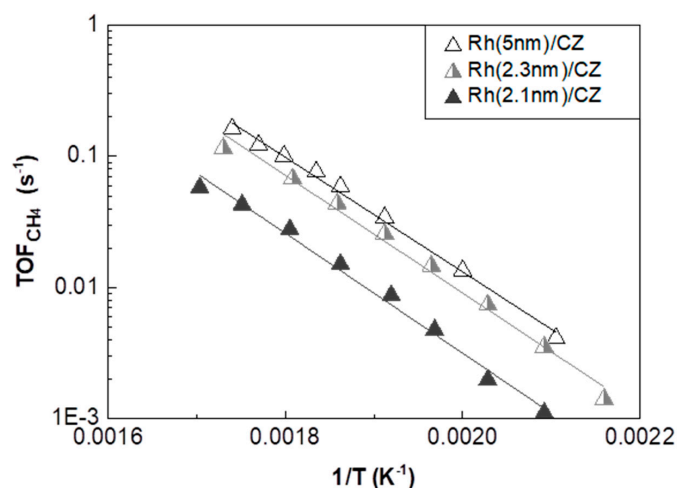

Figure 8. Arrhenius plots of the CH_4 formation turnover frequency (TOF_{CH4}) obtained for Rh/CZ catalysts with different mean Rh particle sizes. Experimental conditions as in Figure 7.

Table 4. Apparent activation energies and pre-exponential factors for CO_2 methanation reaction over Rh/CZ catalysts with different mean Rh particle sizes.

Catalyst	Mean Rh Particle Size (nm)	TOF_{CH4} Apparent Activation Energy (E_a) (kJ/mol)	Pre-Exponential Factor $\left(TOF^o_{CH4}\right)$ (s^{-1})	TOF_{CH4} at T = 280 °C (s^{-1})
Rh(5nm)/CZ	5	83.6 ± 2.5	15.8 ± 0.6	93.6·10^{-3}
Rh(2.3nm)/CZ	2.3	85.8 ± 3.5	16.0 ± 0.8	66.5·10^{-3}
Rh(2.1nm)/CZ	2.1	87.5 ± 3.5	15.3 ± 0.8	27.5·10^{-3}

The above effects are reasonably understood by the following considerations: lower in size dispersed Rh particles correspond to a larger amount of undercoordinated sites, leading to enhanced metal–support interactions. Therefore, as previously discussed, in regard to Figure 2 results, the Rh(5nm)/CZ fresh catalyst inhibiting effect on CO_2 methanation of the very high OSC CZ support, due to over-strengthening of the Rh-CO bond, becomes even worse in the case of smaller particles.

That is, the lower the Rh particles size, the higher the undercoordinated sites and metal–support interactions responsible for reaction inhibition via enhanced CO-poisoning. Indeed, the inhibiting effect is more pronounced on Rh(2.1nm)/CZ and less so on Rh(2.6nm)/CZ, as compared to that on Rh(5nm)/CZ catalysts (Figure 8). Although quite small, the obtained increase in apparent activation energy by decreasing Rh particles size (Table 4) is consistent to the above interpretation. Vulnerability of the CO_2 methanation reaction to CO-poisoning has also been reported by Italiano et al. [22] on Ni/CeO$_2$ catalysts. In addition to the above, strongly bonded CO on Rh surface seems to promote side reaction paths, leading to the formation of a variety of C^{2+} byproducts at the expense of methane formation (Figure 7b,d and Figure 8). It should be noted, however, that the occurrence of these competitive side reactions makes the system more complex and the full understanding of the behavior of the methanation reaction more difficult.

Figure 9 depicts the impact of the support's nature (γ-Al$_2$O$_3$ and CZ) and mean metal particle size on CO_2 methanation intrinsic activity (TOF) of supported Rh nanoparticles, in a comparative manner. The results clearly reveal that the structure sensitivity of CO_2 methanation over Rh is a combined effect of metal–support interactions and particle size: over high OSC capacity support (Rh/CZ catalysts), the reaction is favored by larger particles, in apparent contrast to that obtained over Rh/γ-Al$_2$O$_3$ catalysts (with lack of OSC). The reported here, for the very first time, synergy between the particle size and the OSC characteristic of the support on CO_2 methanation structure sensitivity provides an effective method for promoting catalysts' methanation efficiency via fine-tuning of these two critical parameters (metal particle size and support OSC) during the design of novel effective CO_2 methanation catalyst formulations.

Regarding the most promising in methanation efficiency Rh/ACZ catalyst, investigation of the Rh particle size on its CO_2 methanation activity, similar to that performed for Rh/γ-Al$_2$O$_3$ and Rh/CZ, was not conducted herein. This is because only a very limiting variation on Rh particle size was achieved for Rh/ACZ upon oxidative treatment at 750 and 850 °C (Supplementary Materials Figure S1 and Table S1), making the resulted catalysts unsuitable for such an investigation. Nevertheless, optimization studies focused only on this catalyst, involving preparation of a new series characterized by a wide variation in both Rh particle sizes and OSC values of the ACZ support (the latter to be achievable by changing its CeO$_2$ content) are currently under work. Finally, the time-on-stream stability of Rh/γ-Al$_2$O$_3$, Rh/ACZ, and Rh/CZ catalysts was investigated in 6 h, in stability experiments, under constant feed and temperature conditions. Independently of the support used, the catalysts were very stable (Supplementary Materials Figure S3), confirming the well-known low sintering and coke formation propensity of Rh experienced in close to the present CH$_4$, H$_2$, and CO_2 containing environments at elevated temperatures [53]. It is expected, however, that materials with the ability to provide $O^{\delta-}$ species onto metal particle surfaces (such as ACZ and CZ) add further to catalyst robustness in two ways: oxidizing deposited carbon, and thus preventing carbon accumulation [53],

and preventing particles sintering through the mechanism described in Reference [65]. Although, according to the *sacrificial promoter* concept [66], $O^{\delta-}$ species on the Rh surface are themselves reactive and are rapidly consumed by the oxidizable reactants present (e.g., H_2), they remain nevertheless effective because they are continuously replenished by labile O^{2-} species provided by the support (Equations R3 and R5). At the relatively low temperatures (200–450 °C) advantageous for the CO_2 methanation reaction, the lifetime of $O^{\delta-}$ species is expected to be high enough, and, accordingly, their promotional and anti-sintering effects are significant.
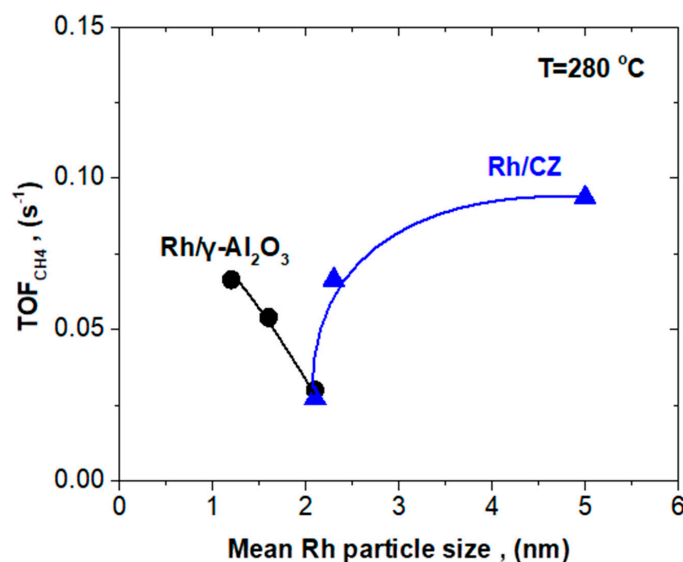
Figure 9. Effect of Rh particle size on the turnover frequency of CO_2 formation (TOF_{CH4}) obtained over Rh/γ-Al_2O_3 and Rh/CZ catalysts at T= 280 °C. Experimental conditions as in Figures 5 and 7 for Rh/γ-Al_2O_3 and Rh/CZ, respectively, and the reaction to be operated at the differential mode (low conversions).

3. Materials and Methods

3.1. Catalysts' Preparation

3.1.1. Supporting Materials

A co-precipitation method [53] was followed for the preparation of ACZ (80 wt % Al_2O_3−20 wt % $Ce_{0.5}Zr_{0.5}O_{2-\delta}$) and CZ ($Ce_{0.5}Zr_{0.5}O_{2-\delta}$) supports in the form of powders, using the corresponding precursor salts: $Al(NO_3)_3 \cdot 9H_2O$, $Zr(NO_3)_2 \cdot H_2O$, and $Ce(NO_3)_3 \cdot 6H_2O$, supplied by Alfa Aesar. The γ-Al_2O_3 support was obtained from Engelhard and was ground to powder (180–250 μm). All supports were calcined at 800 °C, for 1 h, before used for Rh nanoparticles deposition.

3.1.2. Supported Rh Catalysts

Rh nanoparticles were dispersed on the supports via the traditional wet impregnation method, using rhodium (III) nitrate solution (10% *w/v* Rh in 20–25 wt % HNO_3) purchased from Acros Organics as the metal precursor, after its dilution in water, in order to produce a 2 mg Rh/mL concentrated solution of $Rh(NO_3)_3$. Appropriate amounts of each support were impregnated with this solution, under continuous stirring at 75 °C, until water evaporation to yield Rh-supported catalysts with 1.0 wt % Rh nominal loading. The resulted suspensions were dried at 110 °C for 12 h, calcined in air at 450 °C for 1 h (for the nitrate precursor decomposition), and then reduced at 400 °C under 50% H_2/He flow for 2 h, followed by heating (20 °C/min) under 1% H_2/He flow to 800 °C for 1 h, for the removal of any precursors' residuals and structure stabilization. Portions from the as-prepared Rh/γ-Al_2O_3,

Rh/ACZ, and Rh/CZ fresh catalysts were further thermally treated as described below for Rh particle size modification.

3.1.3. Modification of Rh Particle Size

Changes in mean Rh particle size (agglomeration or redispersion) were achieved by further treatment of the fresh Rh/γ-Al$_2$O$_3$ and Rh/CZ catalysts at high-temperature oxidative conditions via the methodology described in detail in Reference [65] (a concise summary of the method is given in the results and discussion section). Two treatment protocols were imposed. Protocol #1: heating in 10 NmL/min flow of 20% O$_2$/He for 2 h at 750 °C, hereafter denoted as "treated at 750 °C" samples. Protocol #2: heating in 10 NmL/min flow of 20% O$_2$/He for 2 h at 750 °C, followed by further heating in the same flow conditions for 2 additional hours, at 850 °C, hereafter denoted as "treated at 850 °C" samples. In this way, a set of seven Rh catalysts, supported on three different OSC supports and with different Rh particle sizes, was achieved that enabled us to a thoroughly investigate the combined effect of these two major material properties (OSC and catalyst particle size) on CO$_2$ methanation. The resulted catalysts are listed in Table 1, using the code Rh(Xnm)/Support, where X denotes mean Rh particle size, and Support is γ-Al$_2$O$_3$, ACZ, or CZ. Catalyst particle-size modification by this method enables a more reliable investigation of the structure sensitivity of the CO$_2$ methanation reaction in light of the advantage of constant metal loading in all the samples under comparison, thus avoiding possible complications created by changing the latter.

3.2. *Characterization Methods*

3.2.1. Materials Characterization

A thorough characterization of the materials (supports and catalysts) was performed by a variety of techniques and has been reported previously [53,65]. However, additional characterizations were also performed herein. Comprehensive details about the methodology followed are provided in the Supplementary Materials (Section S1); a concise summary follows. Total Rh contents were obtained by means of inductively coupled plasma–optical emission spectroscopy (ICP–OES) measurements. Textural, structural, and morphological characteristics of the synthesized catalysts were determined by Brunauer-Emmett-Teller and Barrett-Joyner-Halenda (BET–BJH) method from N$_2$ adsorption–desorption isotherms at −196 °C, high-resolution transmission electron microscopy (HRTEM), and powder X-ray diffraction (PXRD). The *total* oxygen storage capacities (OSC) of the samples were determined by utilizing hydrogen temperature-programmed reduction (H$_2$-TPR) measurements conducted on pre-oxidized samples. Rh particle sizes (d_{Rh}) of the catalysts were determined via HRTEM images and isothermal hydrogen chemisorption experiments; the results were found to be in close agreement. Arithmetic mean values ($\bar{d}_{Rh}$) obtained by the two methods for each catalyst were adopted herein.

3.2.2. Catalytic Performance Evaluation

Catalysts evaluation for the CO$_2$ methanation reaction (R1) was performed in a continuous flow experimental apparatus (Figure 10) consisting of a feed unit, the reactor, and an analysis unit utilizing on-line gas chromatography (SHIMADZU GC-2014, thermal conductivity detector (TCD), Ar carrier gas, equipped with a HayeSep D column), for the analysis of reactants and products. A feed composition of H$_2$/CO$_2$/Ar = 20%/5%/75% at 1 bar, which corresponds to the stoichiometric ratio (H$_2$/CO$_2$ = 4/1) of the reaction (R1), was synthesized in the feed unit of the apparatus, utilizing mass flow meters (MKS-247) connected to cylinders containing the necessary gases, i.e., CO$_2$ (99.6 %), ultra-pure H$_2$, and Ar, and fed to the reactor. The total feed flow rate was adjusted so as to maintain the *effective mean contact time* of the reactants with Rh active sites at the same value (τ(CO$_2$) = 1.26 s; τ(H$_2$) = 5.04 s). Since the various catalytic samples did not actually have an identical number of active sites per mass, the effective contact time is the key parameter that should be kept constant, in order to

obtain rational comparison of their relative merits (at constant wGHSV, the comparison is not actually made on equal terms, due to the differences in the number of active sites that the reactants are exposed to). It is defined as the *surface Rh atoms/(reactant molecules/s)* [56,67] and estimated via Equation (1).

$$\tau(CO_2) = \frac{(w_{cat}X_{Rh}/M_{Rh}) \cdot D_{Rh}}{(F_{in} \cdot [CO_2]_{in}/V_{mol} \cdot 60)} \quad (1)$$

where w_{cat} is the mass (g) of catalyst loaded in the reactor; X_{Rh} is the rhodium content of the catalyst (g_{Rh}/g_{cat}); M_{Rh} is the molecular weight of rhodium (102.9 g/mol); F_{in} (N mL/min) and $[CO_2]_{in}$ (v/v) are the total flow rate and CO_2 concentration in the reactor inlet, respectively; V_{mol} is the molar volume of an ideal gas at room temperature and 1 atm pressure (24,450 N mL/mol); and D_{Rh} is the rhodium dispersion associated with the mean Rh particles sizes ($\bar{d}_{Rh}$), estimated via Equation (2).

$$\bar{d}_{Rh} = \frac{6 \cdot M_{Rh} \cdot 10^{23}}{D_{Rh} \cdot \rho_{Rh} \cdot a_{Rh} \cdot N_{AV}} \quad (2)$$

where $\bar{d}_{Rh}$ is the mean Rh particle size (nm), ρ_{Rh} is the Rh metal density (12.4 g/N mL), a_{Rh} is the area occupied by a surface Rh atom (7.58 Å^2/atom), N_{AV} is the Avogadro number (6.023·10^{23} molecules/mol), and 10^{23} is a unit conversion factor when the units of parameters in Equation (2) are used as indicated above.
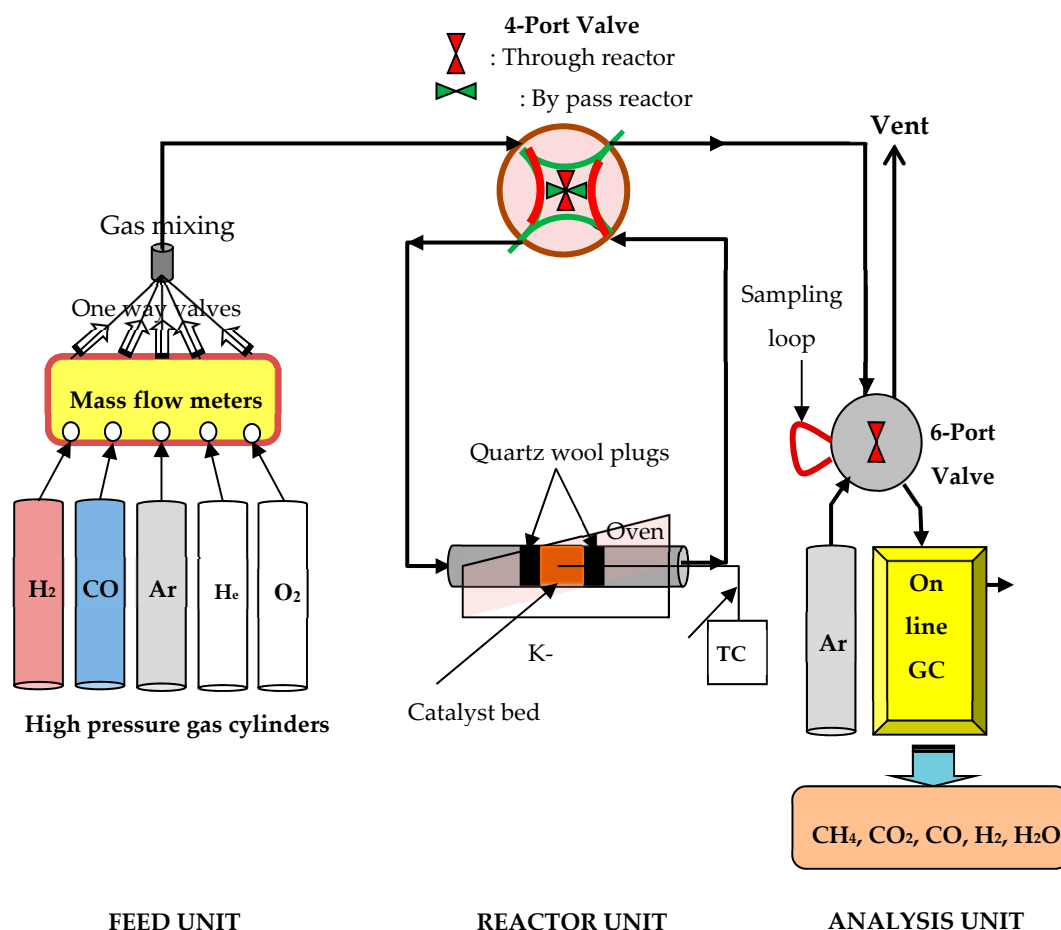

Figure 10. Schematic diagram of the continuous flow experimental apparatus used for catalyst performance evaluation.

A 3 mm internal diameter tubular quartz, fixed bed, single-pass flow reactor was equipped in the apparatus (Figure 10) for the catalytic performance data acquisition, which was loaded, in all cases,

with 50 mg of catalyst (grain size 180–250 μm), held between two quartz wool plugs; the catalyst temperature was measured by a centered K-type thermocouple (Figure 10).

In order to keep $\tau(CO_2)$ at 1.26 s for all catalysts with different concentration of active sites per mass tested, the total feed flow rate (F_{in}) was accordingly varied between 20 and 100 NmL/min, corresponding to weight-basis gas hourly space velocity (wGHSV = F_{in}/w_{cat}) variation into the interval 24,000 to 120,000 NmL/g$_{cat}$ h.

The following equations were used to calculate CO_2 conversion (X_{CO2}), CH_4 and CO yields (Y_{CH4}, Y_{CO}), and corresponding selectivities (S_{CH4}, S_{CO}):

$$X_{CO2} \ (\%) = 100 \cdot (F_{in} \cdot [CO_2]_{in} - F_{out} \cdot [CO_2]_{out})/F_{in} \cdot [CO_2]_{in} \tag{3a}$$

$$Y_{CH4} \ (\%) = 100 \cdot F_{out} \cdot [CH_4]_{out}/F_{in} \cdot [CO_2]_{in} \tag{3b}$$

$$Y_{CO} \ (\%) = 100 \cdot F_{out} \cdot [CO]_{out}/F_{in} \cdot [CO_2]_{in} \tag{3c}$$

$$S_{CH4} \ (\%) = 100 \cdot [CH_4]_{out}/(F_{in} \cdot [CO_2]_{in} - F_{out} \cdot [CO_2]_{out}) \tag{3d}$$

$$S_{CO} \ (\%) = 100 \cdot [CO]_{out}/(F_{in} \cdot [CO_2]_{in} - F_{out} \cdot [CO_2]_{out}) \tag{3e}$$

where F_{in} and F_{out} are the total flow rates in the inlet and outlet of the reactor (NmL/min), respectively; the symbols in brackets are the concentrations (*v/v*) of the corresponding reactants and products.

Based on the above definitions of the reaction output parameters, the following equation was used to check the carbon balance during kinetic experiments:

$$X_{CO2} = Y_{CH4} + Y_{CO} \tag{4}$$

Equation (4) was found to close well with a deviation of less than 3% for the vast majority of kinetic experiments, indicating that CH_4 and CO were the main CO_2 hydrogenation products over the catalysts studied and under the experimental conditions employed.

Attention was paid to both integral (high conversions; light-off performance) and differential (low conversions; intrinsic activity) operation of the reactor, for a better analysis and understanding of the catalytic behavior. Turnover frequency calculations of CH_4 formation, TOF_{CH4} (s^{-1}), defined as *molecules of CH_4 produced per surface Rh atom per second* (Equation (5)), were based on data obtained at low CO_2 and H_2 conversions (ca. 5–15%; differential operation):

$$r_{CH4} = \frac{F_{out} \cdot [CH_4]_{out}}{w_{cat}} \tag{5}$$

where r_{CH4} (mol/g$_{cat}$.s) is the intrinsic rate of CO_2 consumption obtained under differential reactor operation and calculated by using Equation (6):

$$TOF_{CH4}(s^{-1}) = \frac{r_{CH4} \cdot M_{Rh}}{D_{Rh} \cdot X_{Rh}} \tag{6}$$

A combination of Equations (1), (3b), (5), and (6) finally provides the following:

$$TOF_{CH4}(s^{-1}) = \frac{Y_{CH4}(\%)/100}{\tau(CO_2)} \tag{7}$$

4. Conclusions

A detailed investigation of the effect of the support, in regards to its oxygen storage capacity (OSC)/lability and catalyst particle size on important catalytic parameters (light-off characteristics, turnover activity, yield, and selectivity), relevant to CO_2 hydrogenation reaction, on supported Rh nanoparticles, was conducted. This enabled an in-depth understanding of the combined effect of these

important catalyst properties on the titled reaction output characteristics. Different oxide supports, namely γ-Al_2O_3, ACZ, and CZ, with marginal, intermediate, and high oxygen ion lability, were used, over which the same loading (but different in crystallite size) of Rh nanoparticles was dispersed.

The results unambiguously show that OSC of the support is a significant catalyst property that can effectively determine the CO_2 methanation behavior of Rh. Specifically, supports with intermediate OSC values offer optimal CO_2 methanation performance. The *effective double layer* model of metal–support interactions, i.e., the spontaneously created $O^{\delta-}$ layer on the surface of Rh particles via O^{2-} backspillover from supports with high oxygen lability and its concomitant effect on Rh-CO bond strength, fits well with the observations. This effect also accounts for the final competition result between the methanation and reverse water–gas shift reactions during CO_2 hydrogenation.

The structure sensitivity of the Rh-catalyzed CO_2 methanation reaction is confirmed to be a combined result of OSC of the support and mean Rh particle size, capable of being inversed on the same metal, depending on the oxygen lability characteristic of the support: CO_2 methanation efficiency is favored on smaller Rh particles when dispersed on support with lack of oxygen ion lability (Rh/γ-Al_2O_3 catalyst), in full contrast to Rh particles dispersed on support with high oxygen ion lability (Rh/CZ), where the reaction is strongly favored on larger Rh particles.

Some new insights and a sense of awareness can be offered by these findings, which appear highly promising for rational design of CO_2 methanation catalysts; the simultaneous tailoring of support OSC and active phase particle size characteristics of the catalysts enables fine-tuning and optimization of their CO_2 methanation efficiency and selectivity, gaining merits and benefits on a process aiming to control greenhouse gas and renewable fuel production.

References

1. Wang, W.; Wang, S.P.; Ma, X.B.; Gong, J.L. Recent advances in catalytic hydrogenation of carbon dioxide. *Chem. Soc. Rev.* **2011**, *40*, 3703–3727. [CrossRef]
2. Ye, R.P.; Ding, J.; Gong, W.; Argyle, M.D.; Zhong, Q.; Wang, Y.; Russell, C.K.; Xu, Z.; Russell, A.G.; Li, Q.; et al. CO_2 hydrogenation to high-value products via heterogeneous catalysis. *Nat. Comm.* **2019**, *10*, 5698. [CrossRef]
3. Liu, M.; Yi, Y.; Wang, L.; Guo, H.; Bogaerts, A. Hydrogenation of Carbon Dioxide to Value-Added Chemicals by Heterogeneous Catalysis and Plasma Catalysis. *Catalysts* **2019**, *9*, 275. [CrossRef]
4. Vogt, C.; Monai, M.; Kramer, G.J.; Weckhuysen, B.M. The renaissance of the Sabatier reaction and its applications on Earth and in space. *Nat. Catal.* **2019**, *2*, 188–197. [CrossRef]
5. Tsiotsias, A.I.; Charisiou, N.D.; Yentekakis, I.V.; Goula, M.A. The Role of Alkali and Alkaline Earth Metals in the CO_2 Methanation Reaction and the Combined Capture and Methanation of CO_2. *Catalysts* **2020**, *10*, 812. [CrossRef]

6. Frontera, P.; Macario, A.; Ferraro, M.; Antonucci, P. Supported catalysts for CO_2 methanation: A review. *Catalysts* **2017**, *7*, 59. [CrossRef]

7. Aziz, M.A.A.; Jalil, A.A.; Triwahyono, S.; Ahmad, A. CO_2 methanation over heterogeneous catalysts: Recent progress and future prospects. *Green Chem.* **2015**, *17*, 2647–2663. [CrossRef]

8. Baraj, E.; Vagaský, S.; Hlinčík, T.; Ciahotný, K.; Tekáč, V. Reaction mechanisms of carbon dioxide methanation. *Chem. Pap.* **2016**, *70*, 395–403. [CrossRef]

9. Pan, S.Y.; Chiang, P.C.; Pan, W.; Kim, H. Advances in state-of-art valorization technologies for captured CO_2 toward sustainable carbon cycle. *Crit. Rev. Env. Sci. Technol.* **2018**, *48*, 471–534. [CrossRef]

10. Yentekakis, I.V.; Goula, G. Biogas management: Advanced utilization for production of renewable energy and added-value chemicals. *Front. Environ. Sci.* **2017**, *5*, 7. [CrossRef]

11. Ghaiba, K.; Ben-Faresb, F.-Z. Power-to-Methane: A state-of-the-art review. *Renew. Sustain. Energy Rev.* **2018**, *81*, 433–446. [CrossRef]

12. Mazza, A.; Bompard, E.; Chicco, G. Applications of power to gas technologies in emerging electrical systems. *Renew. Sustain. Energy Rev.* **2018**, *92*, 794–806. [CrossRef]

13. Gotz, M.; Lefebvre, J.; Mors, F.; McDaniel Koch, A.; Graf, F.; Bajohr, S.; Reimert, R.; Kolb, T. Renewable Power-to-Gas: A technological and economic review. *Renew. Energy* **2016**, *85*, 1371–1390. [CrossRef]

14. O'Shea, R.; Wall, D.M.; McDonagh, S.; Murphy, J.D. The potential of power to gas to provide green gas utilising existing CO_2 sources from industries, distilleries and wastewater treatment facilities. *Renew. Energy* **2017**, *114*, 1090–1100. [CrossRef]

15. Bonura, G.; Cordaro, M.; Cannilla, C.; Arena, F.; Frusteri, F. The changing nature of the active site of Cu-Zn-Zr catalysts for the CO_2 hydrogenation reaction to methanol. *Appl. Catal. B* **2014**, *152–153*, 152–161. [CrossRef]

16. Dasireddy, V.D.B.C.; Likozar, B. The role of copper oxidation state in $Cu/Zn/Al_2O_3$ catalysts in CO_2 hydrogenation and methanol productivity. *Renew. Energy* **2019**, *140*, 452–460. [CrossRef]

17. Li, M.; Amari, H.; Van Veen, A.C. Metal-oxide interaction enhanced CO_2 activation in methanation over ceria supported nickel nanocrystallites. *Appl. Catal. B* **2018**, *239*, 27–35. [CrossRef]

18. Ye, R.P.; Li, Q.; Gong, W.; Wang, T.; Razink, J.J.; Lin, L.; Qin, Y.Y.; Zhou, Z.; Adidharma, H.; Tang, J.; et al. High-performance of nanostructured Ni/CeO_2 catalyst on CO_2 methanation. *Appl. Catal. B* **2020**, *268*, 118475. [CrossRef]

19. Winter, L.R.; Chen, R.; Chen, X.; Chang, K.; Liu, Z.; Senenayake, S.D.; Ebrahim, A.M.; Chen, J.G. Elucidating the roles of metallic Ni and oxygen vacancies in CO_2 hydrogenation over Ni/CeO_2 using isotope exchange and in situ measurements. *Appl. Catal. B* **2019**, *245*, 360–366. [CrossRef]

20. Winter, L.R.; Gomez, E.; Yan, B.; Yao, S.; Chen, J.G. Tuning Ni-catalyzed CO_2 hydrogenation selectivity via Ni-ceria support interactions and Ni-Fe bimetallic formation. *Appl. Catal. B* **2018**, *224*, 442–450. [CrossRef]

21. Cerda, M.C.; Chica, A.; Keller, S.; Rautenberg, C.; Bentrup, U. Ni-sepiolite and Ni-todorokite as efficient CO_2 methanation catalysts: Mechanistic insight by operando DRIFTS. *Appl. Catal. B* **2020**, *264*, 118546. [CrossRef]

22. Italiano, C.; Llorca, J.; Pino, L.; Farraro, M.; Antonucci, V.; Vita, A. CO and CO_2 methanation over Ni catalysts supported on CeO_2, Al_2O_3 and Y_2O_3 oxides. *Appl. Catal. B* **2020**, *264*, 118494. [CrossRef]

23. Tada, S.; Shimizu, T.; Kameyama, H.; Haneda, T.; Kikuchi, R. Ni/CeO_2 catalysts with high CO_2 methanation activity and high CH_4 selectivity at low temperatures. *Int. J. Hydrog. Energy* **2012**, *37*, 5527–5531. [CrossRef]

24. Liu, H.; Zou, X.; Wang, X.; Lou, X.; Ding, W. Effect of CeO_2 addition on Ni/Al_2O_3 catalysts for methanation of carbon dioxide with hydrogen. *J. Nat. Gas Chem.* **2012**, *21*, 703–707. [CrossRef]

25. Zhu, H.; Razzaq, R.; Li, C.; Muhmmad, Y.; Zhang, S. Catalytic methanation of carbon dioxide by active oxygen material $Ce_xZr_{1-x}O_2$ supported Ni-Co bimetallic nanocatalysts. *AIChE J.* **2013**, *59*, 2567–2576. [CrossRef]

26. Alcalde-Santiago, V.; Davó-Quiñonero, A.; Lozano-Castelló, D.; Quindimil, A.; De-La-Torre, U.; Pereda-Ayo, B.; González-Marcos, J.A.; González-Velasco, J.R.; Bueno-López, A. Ni/LnO_x catalysts (Ln = La, Ce or Pr) for CO_2 methanation. *ChemCatChem* **2019**, *11*, 810–819. [CrossRef]

27. Cárdenas, A.A.; Quindimil, A.; Davó, Q.A.; Bailón, G.E.; Lozano, C.D.; De, L.T.U.; Pereda, A.B.; González, M.J.A.; González, V.J.R.; Bueno, L.A. Design of active sites in Ni/CeO_2 catalysts for the methanation of CO_2: Tailoring the $Ni-CeO_2$ contact. *Appl. Mater. Today* **2020**, *19*, 100591. [CrossRef]

28. Yuan, H.; Zhu, X.; Han, J.; Wang, H.; Ge, Q. Rhenium-promoted selective CO_2 methanation on Ni-based catalyst. *J. CO2 Util.* **2018**, *26*, 8–18. [CrossRef]

29. Ray, K.; Deo, G. A potential descriptor for the CO_2 hydrogenation to CH_4 over Al_2O_3 supported Ni and Ni-based alloy catalysts. *Appl. Catal. B* **2017**, *218*, 525–537. [CrossRef]

30. Weatherbee, G.D.; Bartholomew, C.H. Hydrogenation of CO$_2$ on group VIII metals. IV. Specific activities and selectivities of silica-supported Co, Fe and Ru. *J. Catal.* **1984**, *87*, 352–362. [CrossRef]

31. Kirchner, J.; Anolleck, J.K.; Lösch, H.; Kureti, S. Methanation of CO$_2$ on Iron based catalysts. *Appl. Catal. B* **2018**, *223*, 47–59. [CrossRef]

32. Martin, N.M.; Velin, P.; Skoglundh, M.; Bauer, M.; Carlsson, P.A. Catalytic hydrogenation of CO$_2$ to methane over supported Pd, Rh and Ni catalysts. *Catal. Sci. Technol.* **2017**, *7*, 1086–1094. [CrossRef]

33. Zhang, R.; Liu, H.; Wang, B.; Ling, L. Insights into the effect of surface hydroxyls on CO$_2$ hydrogenation over Pd/γ-Al$_2$O$_3$ catalyst: A computational study. *Appl. Catal. B* **2012**, *126*, 108–120. [CrossRef]

34. Janke, C.; Duyar, M.S.; Hoskins, M.; Farrauto, R. Catalytic and adsorption studies for the hydrogenation of CO$_2$ to methane. *Appl. Catal. B* **2014**, *152–153*, 184–191. [CrossRef]

35. Panagiotopoulou, P. Hydrogenation of CO$_2$ over supported noble metal catalysts. *Appl. Catal. A* **2017**, *542*, 63–70. [CrossRef]

36. Kattel, S.; Yan, B.; Chen, J.G.; Liu, P. CO$_2$ hydrogenation on Pt, Pt/SiO$_2$ and Pt/TiO$_2$: Importance of synergy between Pt and oxide support. *J. Catal.* **2016**, *343*, 115–126. [CrossRef]

37. Kwak, J.H.; Kovarik, L.; Szanyi, J. Heterogeneous catalysis on atomically dispersed supported metals: CO$_2$ reduction on multifunctional Pd catalysts. *ACS Catal.* **2013**, *3*, 2094–2100. [CrossRef]

38. Wang, X.; Shi, H.; Kwak, J.H.; Szanyi, J. Mechanism of CO$_2$ Hydrogenation on Pd/Al$_2$O$_3$ Catalysts: Kinetics and Transient DRIFTS-MS Studies. *ACS Catal.* **2015**, *5*, 6337–6349. [CrossRef]

39. Beuls, A.; Swalus, C.; Jacquemin, M.; Heyen, G.; Karelovic, A.; Ruiz, P. Methanation of CO$_2$: Further insight into the mechanism over Rh/γ-Al$_2$O$_3$ catalyst. *Appl. Catal. B* **2012**, *113–114*, 2–10. [CrossRef]

40. Karelovic, A.; Ruiz, P. CO$_2$ hydrogenation at low temperature over Rh/γ-Al$_2$O$_3$ catalysts: Effect of the metal particle size on catalytic performances and reaction mechanism. *Appl. Catal. B* **2012**, *113–114*, 237–249. [CrossRef]

41. Zhang, Z.; Kladi, A.; Verykios, X.E. Effects of carrier doping on kinetic parameters of CO$_2$ hydrogenation on supported rhodium catalysts. *J. Catal.* **1994**, *148*, 737–747. [CrossRef]

42. Theleritis, D.; Souentie, S.; Siokou, A.; Katsaounis, A.; Vayenas, C.G. Hydrogenation of CO$_2$ over Ru/YSZ electropromoted catalysts. *ACS Catal.* **2012**, *2*, 770–780. [CrossRef]

43. Kalaitzidou, I.; Makri, M.; Theleritis, D.; Katsaounis, A.; Vayenas, C.G. Comparative study of the electrochemical promotion of CO$_2$ hydrogenation on Ru using Na$^+$, K$^+$, H$^+$ and O^{2-} conducting solid electrolytes. *Surf. Sci.* **2016**, *646*, 194–203. [CrossRef]

44. Li, S.; Xu, Y.; Chen, Y.; Li, W.; Lin, L.; Li, M.; Deng, Y.; Wang, X.; Ge, B.; Yang, C.; et al. Tuning the Selectivity of Catalytic Carbon Dioxide Hydrogenation over Iridium/Cerium Oxide Catalysts with a Strong Metal–Support Interaction. *Angew. Chem. Int. Ed.* **2017**, *56*, 10761–10765. [CrossRef]

45. Xu, J.; Su, X.; Duan, H.; Hou, B.; Lin, Q.; Liu, X.; Pan, X.; Pei, G.; Geng, H.; Huang, Y.; et al. Influence of pretreatment temperature on catalytic performance of rutile TiO$_2$-supported ruthenium catalyst in CO$_2$ methanation. *J. Catal.* **2016**, *333*, 227–237. [CrossRef]

46. Petala, A.; Panagiotopoulou, P. Methanation of CO$_2$ over alkali-promoted Ru/TiO$_2$ catalysts: I. Effect of alkali additives on catalytic activity and selectivity. *Appl. Catal. B* **2018**, *224*, 919–929. [CrossRef]

47. Panagiotopoulou, P.; Verykios, X.E. Mechanistic Study of the Selective Methanation of CO over Ru/TiO$_2$ Catalysts: Effect of Metal Crystallite Size on the Nature of Active Surface Species and Reaction Pathways. *J. Phys. Chem. C* **2017**, *121*, 5058–5068. [CrossRef]

48. Agnelli, M.; Swaan, H.M.; Marquez-Alvarez, C.; Martin, G.A.; Mirodatos, C. CO Hydrogenation on a Nickel Catalyst II. A Mechanistic Study by Transient Kinetics and Infrared Spectroscopy. *J. Catal.* **1998**, *175*, 117–128. [CrossRef]

49. Charisiou, N.D.; Siakavelas, G.; Tzounis, L.; Sebastian, V.; Monzon, A.; Baker, M.A.; Hinder, S.J.; Polychronopoulou, K.; Yentekakis, I.V.; Goula, M.A. An in depth investigation of deactivation through carbon formation during the biogas dry reforming reaction for Ni supported on modified with CeO$_2$ and La$_2$O$_3$ zirconia catalysts. *Int. J. Hydrog. Energy* **2018**, *43*, 18955–18976. [CrossRef]

50. Goula, M.A.; Charisiou, N.D.; Siakavelas, G.; Tzounis, L.; Tsiaoussis, I.; Panagiotopoulou, P.; Goula, G.; Yentekakis, I.V. Syngas production via the biogas dry reforming reaction over Ni supported on zirconia modified with CeO$_2$ or La$_2$O$_3$ catalysts. *Int. J. Hydrog. Energy* **2017**, *42*, 13724–13740. [CrossRef]

51. Ashcroft, A.T.; Cheetham, A.K.; Green, M.L.H.; Vernon, P.D.F. Partial oxidation of methane to synthesis gas using carbon dioxide. *Nature* **1991**, *352*, 225–226. [CrossRef]

52.　Yentekakis, I.V.; Goula, G.; Panagiotopoulou, P.; Katsoni, A.; Diamadopoulos, E.; Mantzavinos, D.; Delimitis, A. Dry Reforming of Methane: Catalytic Performance and Stability of Ir Catalysts Supported on γ-Al_2O_3, $Zr_{0.92}Y_{0.08}O_{2-\delta}$ (YSZ) or $Ce_{0.9}Gd_{0.1}O_{2-\delta}$ (GDC) Supports. *Top. Catal.* **2015**, *58*, 1228–1241. [CrossRef]

53.　Yentekakis, I.V.; Goula, G.; Hatzisymeon, M.; Betsi-Argyropoulou, I.; Botzolaki, G.; Kousi, K.; Kondarides, D.I.; Taylor, M.J.; Parlett, C.M.A.; Osatiashtiani, A.; et al. Effect of support oxygen storage capacity on the catalytic performance of Rh nanoparticles for CO_2 reforming of methane. *Appl. Catal. B* **2019**, *243*, 490–501. [CrossRef]

54.　Yentekakis, I.V.; Vernoux, P.; Goula, G.; Caravaca, A. Electropositive promotion by alkalies or alkaline earths of Pt-group metals in emission control catalysis: A status Report. *Catalysts* **2019**, *9*, 157. [CrossRef]

55.　Konsolakis, M.; Drosou, C.; Yentekakis, I.V. Support mediated promotional effects of rare earth oxides (CeO_2 and La_2O_3) on N_2O decomposition and N_2O reduction by CO or C_3H_6 over Pt/Al_2O_3 structured catalysts. *Appl. Catal. B* **2012**, *123–124*, 405–413. [CrossRef]

56.　Yentekakis, I.V.; Tellou, V.; Botzolaki, G.; Rapakousios, I.A. A comparative study of the C_3H_6 + NO + O_2, C_3H_6 + O_2 and NO + O_2 reactions in excess oxygen over Na-modified Pt/γ-Al_2O_3 catalysts. *Appl. Catal. B* **2005**, *56*, 229–239. [CrossRef]

57.　Vayenas, C.G.; Bebelis, S.; Yentekakis, I.V.; Lintz, H.-G. Non-faradaic electrochemical modification of catalytic activity: A status report. *Catal. Today* **1992**, *11*, 303–438. [CrossRef]

58.　Yang, X.-F.; Wang, A.; Qiao, B.; Li, J.; Liu, J.; Zhang, T. Single-atom catalysts: A new frontier in heterogeneous catalysis. *Acc. Chem. Res.* **2013**, *46*, 1740–1748. [CrossRef]

59.　Akri, M.; Zhao, S.; Li, X.; Zang, K.; Lee, A.F.; Isaacs, M.A.; Xi, W.; Gangarajula, Y.; Luo, J.; Ren, Y.; et al. Atomically dispersed nickel as coke-resistant active sites for methane dry reforming. *Nat. Commun.* **2019**, *10*, 5181. [CrossRef]

60.　Montini, T.; Melchionna, M.; Monai, M.; Forniasiero, P. Fundamentals and Catalytic Applications of CeO_2-based Materials. *Chem. Rev.* **2016**, *116*, 5987–6041. [CrossRef]

61.　He, H.; Dai, H.X.; Au, C.T. Defective structure, oxygen mobility, oxygen storage capacity, and redox properties of RE-based (RE= Ce, Pr) solid solutions. *Catal. Today* **2004**, *90*, 245–254. [CrossRef]

62.　Yentekakis, I.V.; Konsolakis, M. Three-way Catalysis (Book Chapter). In *Perovskites and Related Mixed Oxides: Concepts and Applications*; Wiley-VCH, Vergal GmbH & Co. KGaA: Weinheim, Germany, 2016; pp. 559–586.

63.　Bunluesin, T.; Gorte, R.J.; Graham, G.W. Studies of the Water-Gas-Shift Reaction on Ceria-Supported Pt, Pd, and Rh: Implications for Oxygen-Storage Properties. *Appl. Catal. B* **1998**, *15*, 107–114. [CrossRef]

64.　Yentekakis, I.V.; Goula, G.; Panagiotopoulou, P.; Kampouri, S.; Taylor, M.J.; Kyriakou, G.; Lambert, R.M. Stabilization of catalyst particles against sintering on oxide supports with high oxygen ion lability exemplified by Ir-catalyzed decomposition of N_2O. *Appl. Catal. B* **2016**, *192*, 357–364. [CrossRef]

65.　Goula, G.; Botzolaki, G.; Osatiashtiani, A.; Parlett, C.M.A.; Kyriakou, G.; Lambert, R.M.; Yentekakis, I.V. Oxidative thermal sintering and redispersion of Rh nanoparticles on supports with high oxygen ion lability. *Catalysts* **2019**, *9*, 541. [CrossRef]

66.　Vayenas, C.G.; Brosda, S.; Pliangos, C. The double-layer approach to promotion, electrocatalysis, electrochemical promotion, and metal–support interactions. *J. Catal.* **2003**, *216*, 487–504. [CrossRef]

67.　Yentekakis, I.V.; Lambert, R.M.; Konsolakis, M.; Kiousis, V. The effect of sodium on the Pd-catalyzed reduction of NO by methane. *Appl. Catal. B* **1998**, *18*, 293–305. [CrossRef]

68.　Fornasiero, P.; Dimonte, R.; Ranga Rao, G.; Kaspar, J.; Meriani, S.; Trovarelli, A.; Graziani, M. Rh-loaded CeO_2-ZrO_2 solid-solutions as highly efficient oxygen exchangers: Dependence of the reduction behavior and the oxygen storage capacity on the structural properties. *J. Catal.* **1995**, *151*, 168–177. [CrossRef]

69.　Ozawa, M.; Takahashi-Morita, M.; Kobayashi, K.; Haneda, M. Core-shell type ceria zirconia support for platinum and rhodium three way catalysts. *Catal. Today* **2017**, *281*, 482–489. [CrossRef]

70.　Zhao, B.; Ran, R.; Cao, Y.; Wu, X.; Weng, D.; Fan, J.; Wu, X. Insight into the effects of different ageing protocols on Rh/Al_2O_3 catalysts. *Appl. Surf. Sci.* **2014**, *308*, 230–236. [CrossRef]

71.　Hori, C.E.; Permana, H.; Simon Ng, K.Y.; Brenner, A.; More, K.; Rahmoeller, K.M.; Belton, D. Thermal stability of oxygen storage properties in a mixed CeO_2-ZrO_2 system. *Appl. Catal. B* **1998**, *16*, 105–117. [CrossRef]

72.　Trovarelli, A.; Mustazza, C.; Dolcetti, G. Carbon dioxide hydrogenation on rhodium supported on transition metal oxides. Effect of reduction temperature on product distribution. *Appl. Catal.* **1990**, *65*, 129–142. [CrossRef]

73.　Solymosi, F.; Erdöhelyi, A.; Bánsági, T. Methanation of CO_2 on supported rhodium catalyst. *J. Catal.* **1981**, *68*, 371–382. [CrossRef]

74. Pliangos, A.; Yentekakis, I.V.; Papadakis, V.G.; Vayenas, C.G.; Verykios, X.E. Support-induced promotional effects on the activity of automotive exhaust catalysts: 1. The case of oxidation of light hydrocarbons (C_2H_4). *Appl. Catal. B* **1997**, *14*, 161–173. [CrossRef]

75. Vayenas, C.G.; Brosda, S. Electron donation–backdonation and the rules of catalytic promotion. *Top. Catal.* **2014**, *57*, 1287–1301. [CrossRef]

76. Lizarraga, L.; Souentie, S.; Mazri, L.; Billard, A.; Vernoux, P. Investigation of the CO oxidation rate oscillations using electrochemical promotion of catalysis over sputtered-Pt films interfaced with YSZ. *Electroch. Commun.* **2020**, *12*, 1310–1313. [CrossRef]

77. Amsler, J.; Sarma, B.B.; Agostini, G.; Prieto, G.; Plessow, P.N.; Studt, F. Prospects of heterogeneous hydroformylation with supported single atom catalysts. *J. Am. Chem. Soc.* **2020**, *142*, 5087–5096. [CrossRef] [PubMed]